J. Fluid Mech. (2002), *vol.* 468, *pp.* 29–75.
DOI: 10.1017/S0022112002001519 Printed in the United Kingdom

Mixing enhancement via the release of strongly nonlinear longitudinal Görtler vortices and their secondary instabilities into the mixing region

By I. G. GIRGIS† AND J. T. C. LIU

Division of Engineering and the Center for Fluid Mechanics, Brown University, Providence, RI 02912, USA
Joseph_Liu@brown.edu

(Received 8 August 2001 and in revised form 11 April 2002)

Mixing enhancement in a mixing layer is considered in terms of a 'vortex generator' that uses fluid dynamically generated counter-rotating longitudinal vortices rather than explicit winglets or similar devices. This view is reached through considering the centrifugal instability of weak initial Görtler vortices on a slightly concave wall that are allowed to develop to their various nonlinear stages through selecting the cutoff lengths of the trailing edge prior to their release into the mixing region. These vortices are released from one side of the (say, upper) stream in the present work. The quantitative entrainment properties of the longitudinal vortices are studied to select an optimal trailing-edge cutoff for fixed upstream conditions. As the vortices develop along the wall, they are intensified because of the centrifugal instability mechanism and because of the work done by the Reynolds stress of the vortices against the local mean flow rate of strain; simultaneously, the region of strong streamwise vorticity moves away from the wall. This selection process is explained through a balance between the vorticity strength and proximity to the lower stream when the trailing edge is cut off: it is shown, therefore, that vortices of relatively modest strength and kinetic energy that are close to the interface separating the two streams provide mixing properties superior to stronger vortices located too far from the interface. Energy-balancing mechanisms and the stretching of the initial interface are studied, as are the effects of the velocity ratio and the spanwise wavelengths other than the fundamental. In order further to enhance mixing by exploiting the inherent secondary instability of primary steady longitudinal vortices, the most amplified secondary instability of the optimal-trailing-edge cutoff situation, which is the sinuous mode, is studied in detail in terms of the nonlinear development and modification of the steady vortical flow. Local energy-exchange mechanisms are studied, as are the mixing properties of the modified steady flow, which are shown to be significantly improved compared to the unmodified steady flow. Though the initiation of steady longitudinal vortices relies on centrifugal instability upstream, such vortices are able to develop self-sustaining and amplifying properties through the Reynolds stresses in the mixing region even without centrifugal instability reinforcement. The secondary instability is initiated and sustained entirely through its own three-dimensional Reynolds stress properties, which work against the three-dimensional rates of strain in the entire steady flow. This contrasts with initially generated potential-like vortices that decay downstream

† Present address: Department of Mechanical and Aerospace Engineering, Princeton University, Princeton, NJ 08544, USA.

in the presence of dissipative mechanisms without the production mechanisms due to the Reynolds stresses.

1. Introduction

Longitudinal vortices are important in scientific and industrial applications for the enhancement of mixing and scalar transport. The methods of generating such vortices include tabs (Bradbury & Khadem 1975; Zaman, Reeder & Samimy 1994) and winglet-type vortex generators (Fiebig 1996; Carletti & Rogers 1995) inserted into the flow field, lobed wall geometry in exit flows (Crouch, Coughlin & Paynter 1977; Presz, Gousy & Morin 1986; Tillman, Patrick & Paterson 1991; Eckerle, Sheibani & Awad 1992; McCormick 1992; McCormick & Bennett 1994; Yu, Yeo & Teh 1995; Tsui & Wu 1996), ramp nozzles (Yu *et al.* 1992), and swirl generators (Naughton & Settles 1992). Secondary flows and lobed fuel injectors are useful in combustion systems (Schadow *et al.* 1989; Swithenbank *et al.* 1989; Rao & Heiba 1990), particularly to control the sequence of mixing and combustion in order to lower pollutant levels from air-breathing aero-engines (Smith *et al.* 1997; Strickland, Selerland & Karagozian 1998).

DeBonis (1992) simulated the flow field of a two-dimensional mixer ejector nozzle. The temperature profiles obtained showed mushroom-like structures in the iso-temperature contours that strongly resemble the iso-streamwise velocity contours in Görtler vortices, as expected from similarity considerations, at least for an incompressible flow (Liu & Sabry 1991). Waitz *et al.* (1997) present a review, primarily of work associated with that thirteen-author paper. Grosch *et al.* (1997) numerically simulated the presence of small tabs in a hot supersonic two-dimensional jet, using an empirical relation to model the tabs by introducing as upstream condition a pair of incompressible counter-rotating vortices. As expected, these steady flow simulations showed that mixing was enhanced.

Goldstein & Mathew (1993) made a theoretical study of the effect of weak streamwise vortices in the free stream on the mixing layer in the large-Reynolds-number limit. They ignored the upstream boundary layer on the wall. The three-dimensionality of the vortices did not generate strongly nonlinear 'mushroom' structures, as in Lee & Liu (1992). In the present problem, in contrast to Goldstein & Mathew (1993), the wall boundary layer is essential to the development of the initial conditions for the mixing region. The nonlinear advection effect of the longitudinal vortices in contorting the iso-scalar lines at the start of the mixing layer, and its subsequent nonlinear development in the free-flow region, bring into contact significant additional surface areas of the two fluids for enhanced entrainment and mixing.

The insertion of objects into the flow and the deformation of trailing edges for longitudinal vorticity generation will undoubtedly introduce associated penalties in applications of thrust loss, form and skin-friction drag increase and increased pressure drop requirements. Zaman *et al.* (1994) concluded that the net thrust loss is about 1% to 1.5% per tab. The skin-friction losses over lobed mixers are undoubtedly greater that those on a flat plate because of increased surface area. This realization suggests the exploration of mixing enhancement through longitudinal vortices arising from flow instabilities rather than from fixed-geometry hardware. In fact, Novopashin & Perepelkin (1989) discussed the importance of 'naturally' occurring longitudinal vortices in mixing enhancement in an underexpanded supersonic jet. These vortices

were induced by roughness inside the nozzle and subsequently amplified by curvature effects in the initial region of the underexpanded jet. The fact that such small vortices can play a large role in mixing enhancement suggests that well-controlled, strongly nonlinear Görtler vortices could be an efficient mechanism for mixing enhancement owing to the transport properties in the cross-sectional plane associated with the mushroom-like iso-streamwise velocity and iso-scalar structures. The infusion of longitudinal vortices, by whatever means, into an otherwise two-dimensional mixing region essentially short-circuits the development of wavy unstable disturbances of the type reviewed by Ho & Huerre (1984) in which the disturbance vorticity axis is normal to the main shear.

It is well-known that longitudinal vortices are also the product of two-dimensional free-shear-flow instabilities, which eventually develop in the downstream region after the development of two-dimensional Kelvin–Helmholtz instabilities, as revealed by the flow visualization studies of Lasheras & Choi (1988); these workers also perturbed the predominantly two-dimensional shear layer by periodically deforming the trailing edge in the streamwise and the normal directions and produced more or less distinct spanwise and streamwise 'vortex tubes'. Wang (1984) studied experimentally the effect of curvature on a mixing layer as it issues into a curved channel. In this case, the two-dimensional instabilities preceded the development of longitudinal vortices attributable to centrifugal instability. Similar experiments were performed by Karasso & Mungal (1997) in a mildly curved liquid shear layer. In general, longitudinal vortices eventually developing from perturbed Kelvin–Helmholtz shear instability are stretched out far downstream in terms of the local momentum or shear layer thicknesses, so that their utility in providing rapid mixing over compact streamwise distances is severely limited. For this reason, curved mixing layers are not the subject of interest here, even in its nonlinear development (this subject, however, has been the subject of studies by numerous other authors (Margolis & Lumley 1965; Liou 1994; Otto, Jackson & Hu 1996)). These predominantly two-dimensional instabilities are in contrast to the present studies, where three-dimensional flow structures and instabilities are developed at the outset and released into the mixing region.

The aim of this paper is to study the use of fluid-dynamically generated longitudinal vortices, initiated before release into the mixing region, in promoting mixing enhancement behind the trailing edge. While the initiation and nonlinear development of the longitudinal vortices in the wall region rely on centrifugal instability, the released vortices sustain themselves via the Reynolds stress energy-conversion mechanism in the free-shear-flow region. This appears to be a novel concept for mixing enhancement that could replace explicit vortex generators and reshaped lobed nozzle exits.

In the present work, the mixing dynamics are dominated by longitudinal vortices of the Görtler type. Through a scale analysis similar to that for wall-bounded flow (Hall 1983, 1988; Floryan & Saric 1982; Saric 1994; Liu & Sabry 1991), a system of parabolized, nonlinear differential equations for the free mixing region is obtained. Although not addressed explicitly, Görtler vortices on the wall upstream are assumed to be generated from a controlled roughness distribution; Denier, Hall & Seddougui (1991) showed how the most amplified linear mode is related to the forcing roughness.

For ease in exposition of the basic concepts, the flow is assumed laminar and incompressible, since coherent structures in turbulent shear flows (Liu 1988) have similar instability mechanisms. Previous work (Liu & Sabry 1991; Liu & Lee 1995) has discussed the analogy between streamwise momentum and scalar transport. The efficiency of mixing is measured through the downstream development of a local mixing efficiency related to the entrainment process, the mixedness parameter and

the stretching of the interfacial surface between fluids originally in the upper and lower streams. The paper has two parts: the first concerns the effect of steady three-dimensional vortices on mixing in which an optimum trailing-edge cutoff is selected, and the second concerns the excitation of secondary instability in the optimal configuration of the steady flow problem and its role in mixing enhancement.

The numerical algorithm for the present problem is developed from the artificial-compressibility method of Chorin (1967); it is used both for recomputing the wall-bounded flow of Lee & Liu (1992) to provide initial conditions for the trailing-edge cutoff and for determining the downstream mixing flow.

The outline of this paper is as follows: the steady flow problem is formulated in § 2; in § 3 the results are given and discussed for the steady flow field structure of the longitudinal vortex in the mixing region for various trailing-edge lengths, and these results are used to optimize the mixing parameters, interfacial length stretching, particle path and the disturbance energy. In § 4 the nonlinear description of secondary instability is formulated, including the scaling leading to simpler parabolic equations. Results for the unsteady problem are presented in § 5, including structural features of the secondary instability, its modification of the steady flow through the Reynolds stresses, mixing enhancement properties, energy-balancing mechanisms, and a sequence of time oscillations of the iso-streamwise velocity contours, similar to iso-scalar contours in flow visualization at a downstream cross-section (Peerhossaini & Wesfried 1988). Concluding remarks and possible extensions appear in § 6.

2. Formulation and discussion of the steady flow problem

The scale analysis leads to nonlinear parabolic partial differential equations for Görtler flows for boundary layers that are thin relative to the radius of a slightly curved wall. This system of equations was given in Floryan & Saric (1982) and Hall (1983, 1988) (see also the review article by Saric 1994).

Since the nonlinearly developed longitudinal vortices from upstream weak Görtler vortices serve as initial conditions for the downstream mixing flow, the scale analysis lead to the same nonlinear parabolic partial differential equations in the mixing region as for the wall-bounded flow upstream of the trailing edge (just as laminar boundary layers and mixing layers are described by the same partial differential equations).

The flow at the end of the slightly curved wall exits tangentially at the trailing edge and thus the Görtler centrifugal mechanism is absent in the mixing region. However, flow inertia or memory would persist through the presence of the nonlinear longitudinal vortices into the mixing region. Unlike potential vortices, the longitudinal vortices in the mixing region are sustained by their three-dimensional Reynolds stresses, which extract energy from and hence modify the basic flow.

The nonlinear momentum problem for the generation of longitudinal vortices in wall-bounded flow is characterized by mushroom-like structures for the total streamwise velocity component (see for instance, Swearingen & Blackwelder 1987; Sabry & Liu 1991; Lee & Liu 1992). It is of interest that, because of the large-Reynolds-number scaling, the streamwise pressure gradient does not appear in the streamwise X-momentum equation, thus rendering it identical to the transport equation for temperature or the binary diffusion equation in incompressible flow (Liu & Sabry 1991). The momentum problem, which is three-dimensional, is nonlinear, but for an incompressible flow the momentum problem is solved first and is then presumed known, so that the heat and mass transport equation is linear (Liu & Lee 1995).

To account conveniently for the upstream boundary-layer effects in the generation

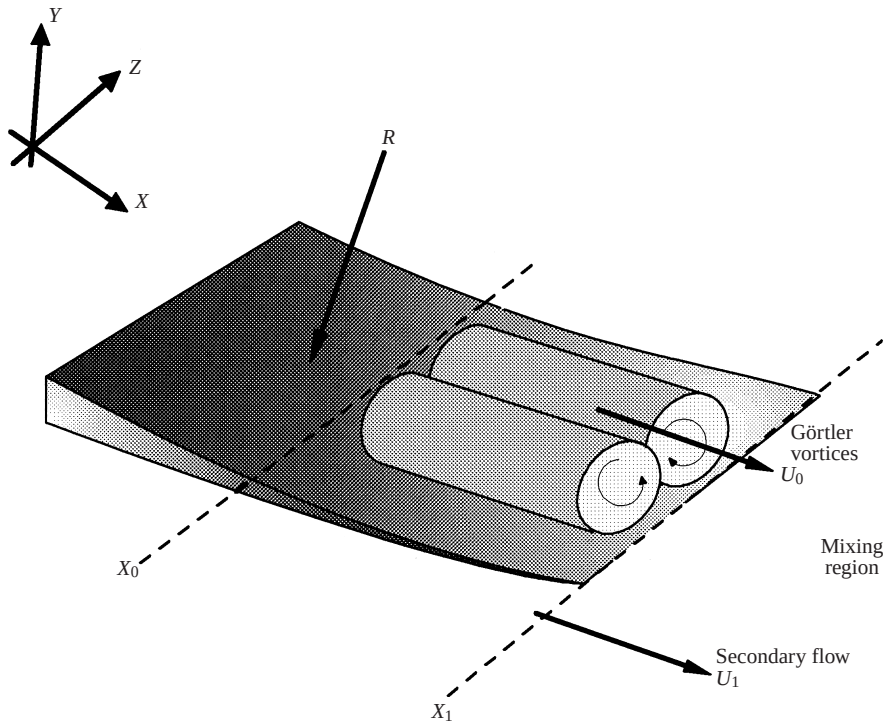

FIGURE 1. Schematic of the mixing enhancement configuration.

of longitudinal vortices, we use the normalizing scales of the wall region for the mixing region. Figure 1 shows a schematic diagram of the nomenclature. The parameters in the momentum problem include the dimensionless wavenumber β, made dimensionless by δ_0, and the Görtler number $G = (U_0\delta_0/\nu)(\delta_0/R)^{1/2}$, where $\delta_0 = (\nu X_0/U_0)^{1/2}$ is a normal length scale, U_0 is the free-stream velocity, ν is the kinematic viscosity and R is the wall radius. In the following, X, Y, Z are the physical streamwise, normal and spanwise coordinates, U, V, W are the corresponding velocity components and P is the pressure; the respective dimensionless quantities are denoted by lower-case symbols:

$$x = \frac{X}{X_0}, \quad y = \frac{Y}{\delta_0}, \quad z = \frac{Z}{\delta_0}, \quad u = \frac{U}{U_0}, \quad v = \left(\frac{V}{U_0}\right)\left(\frac{X_0}{\delta_0}\right),$$

$$w = \left(\frac{W}{U_0}\right)\left(\frac{X_0}{\delta_0}\right), \quad p = \left(\frac{P}{\rho U_0^2}\right)\left(\frac{X_0}{\delta_0}\right)^2, \tag{2.1}$$

where X_0 is the streamwise location at which the initial weak Görtler vortex is initiated. From laminar boundary-layer considerations, the ratio of the two scales δ_0/X_0 is related to the Reynolds number as $(Re_{X_0})^{-1/2}$, where $Re_{X_0} = U_0X_0/\nu$. The scale of the Blasius laminar boundary-layer thickness is about $5\delta_0$ at X_0.

2.1. *Basic equations and boundary conditions*

The basic equations for the nonlinear spatial development of the longitudinal vorticity elements originating from weak upstream Görtler vortices are thoroughly discussed from the present point of view in Sabry & Liu (1991) and Lee & Liu (1992) and

thus will not be treated here; refer to (4.3) to (4.6) but without the Reynolds stresses. The Görtler mechanism in the y-momentum equation is retained in the wall region and is set to zero in the mixing region. The boundary and upstream initial conditions for the wall region are the same as in Sabry & Liu (1991) and Lee & Liu (1992): the upstream conditions are appropriate to initially weak Görtler vortices and were made to satisfy the local linear theory (Floryan & Saric 1982), where the shape of the initial disturbance is consistent with the local Görtler number and wavenumber; the maximum amplitude was established from experimental measurements (e.g. Swearingen & Blackwelder 1987). The strongly nonlinear, spatially developing longitudinal vortices described in Lee & Liu (1992) are then used as upstream initial conditions for the mixing region.

The boundary and upstream initial conditions for the mixing region are

$$u \to 1, \quad \partial v/\partial y \to 0, \quad w \to 0 \quad \text{as} \quad y \to \infty \tag{2.2}$$

in the upper region, representing the 'core region' in nozzle flow, and

$$u \to U_1/U_0, \quad \partial v/\partial y \to 0, \quad w \to 0 \quad \text{as} \quad y \to -\infty \tag{2.3}$$

in the lower region, representing the 'secondary air' region in nozzle flow. The spanwise-periodic boundary condition $\boldsymbol{u}(x, y, 0) = \boldsymbol{u}(x, y, \lambda)$ is the same as that for the wall region, where λ is the dimensionless wavelength normalized by δ_0. The upstream initial condition is given by

$$\boldsymbol{u} = \boldsymbol{u}(x = x_g, y, z), \tag{2.4}$$

where $\boldsymbol{u}(x = x_g, y, z)$ is the longitudinal vortex solution for wall-bounded flow described by Lee & Liu (1992) and x_g is the dimensionless length that the wall-bounded longitudinal vortex must develop on the wall prior to its release into the free mixing region.

2.2. *Computational procedure*

Here the artificial compressibility approach of Chorin (1967) is used, which has been proven, in numerous previous CFD calculations, to have a good convergence rate and high accuracy. The principle of the artificial compressibility method is to add a time derivative of an artificial density, ρ, to the continuity equation. Accordingly, the artificial equation of state is established in order to relate the pressure to the artificial density as: $P = \rho/\Delta$, where Δ is the artificial compressibility. In this way, time is only an auxiliary variable and the final steady solution does not depend on Δ.

The conservative form of the governing equations has been discretized using an explicit finite-difference scheme. Both the x-inertia and time terms are discretized using backward difference formula. A second-order central difference formula was used for the y-inertia, z-inertia, pressure, and viscous terms. To obtain a high convergence rate, the Gauss–Seidel method was utilized in the iteration process, and to ensure solution stability, the time step was limited by the minimum grid spacing and artificial sound speed values. A series of numerical experiments was carried out on the grid size to ensure a grid-independent solution, and we decided on a 102×51 non-uniform grid (to increase the solution accuracy) in the (y, z)-plane for wall-bounded flow and a 204×51 grid for the mixing region. In physical coordinates, the computational grid corresponds to $50\delta_0$ in the Y-direction for wall-bounded flow and $100\delta_0$ in the mixing region. Most of the computation was done on the Ultra Enterprise 5000 machine (1.5 GB memory and 250 MHz UltraSPARC II processor).

In the computational scheme, total flow quantities are used as dependent variables,

as in Sabry & Liu (1991) and Lee & Liu (1992). The mean flow is obtained via spanwise averaging, which is the Reynolds average in the steady flow problem. In the dimensionless variables already defined, the mean of any flow quantity q is

$$\bar{q}(x, y) = \lambda^{-1} \int_0^{\lambda} q(x, y, z)\, \mathrm{d}z.$$

The disturbance velocity is then obtained by subtraction as $q'(x, y, z) = q(x, y, z) - \bar{q}(x, y)$.

The initial condition for the wall-bounded flow is the Blasius solution for the laminar mean flow and the linearized perturbation solution for Görtler vortices. Following standard procedures (e.g. Floryan & Saric 1982), the multiple shooting method was used to solve the boundary value problem of the local linear theory. This system forms an eigenvalue problem for the parameters $\beta = 2\pi/\lambda$, σ and G, where σ is the local spatial amplification rate.

2.3. *The scalar transport problem*

It is possible to infer from the momentum problem the behaviour of scalar quantities such as temperature and concentration through a direct extension to the mixing region of the similarity discussed by Liu & Sabry (1991). For an incompressible flow in the boundary layer, they showed that the uncoupled heat-transfer problem and the binary-diffusion mass-transfer problem are both similar to the streamwise momentum problem in the development of nonlinear longitudinal vortices from weak upstream Görtler vortices. This similarity requires that the Prandtl and Schmidt numbers be unity; the dimensionless initial and boundary conditions must also be similar and the boundary layer must be thin relative to the concave-wall radius. The non-unity Pr and Sc problems, which require numerical computation, are discussed by Liu & Lee (1995).

Because of the streamwise pressure gradient in the secondary instability problem, the analogy with steady flow does not carry through exactly. The similarity may still be applicable in the special case of 'long' streamwise wavelengths compared to the boundary and shear layer thickness. The scalar structures observed even in the unsteady situation (Peerhossaini & Wesfried 1988; Swearingen & Blackwelder 1987) are now understood to be related in some way to the streamwise velocity features, even if the analogy is not strict.

3. Steady flow problem: results and discussion

We first discuss the resulting flow structure for various trailing-edge lengths and mixing enhancement assessments, particle paths, the effect of spanwise wavelength and mixing-region velocity ratio, and energy considerations.

For numerical consistency as well as convenience, the wall-bounded problem is recomputed numerically. The growth of the initially weak Görtler vortices corresponds to parameters for the strongly amplified mode found in the experiments of Swearingen & Blackwelder (1987) and the computational initial conditions of Sabry (1988), Sabry & Liu (1988, 1991), Liu & Domaradzki (1990, 1993) and Liu (1991) for the temporal problem (see also Park (1990) and Park & Huerre (1995) for temporal Görtler vortices in the asymptotic non-growing boundary-layer problem) and Lee & Liu (1992), Benmalek (1993) and Benmalek & Saric (1993) for the spatial problem.

The experimental conditions used are: $U_0 = 5\,\mathrm{m\,s^{-1}}$, $R = 3.2\,\mathrm{m}$ and the spanwise wavelength $\lambda = 1.8\,\mathrm{cm}$ in room temperature air ($Re/\mathrm{cm} = 3425$), with the computa-

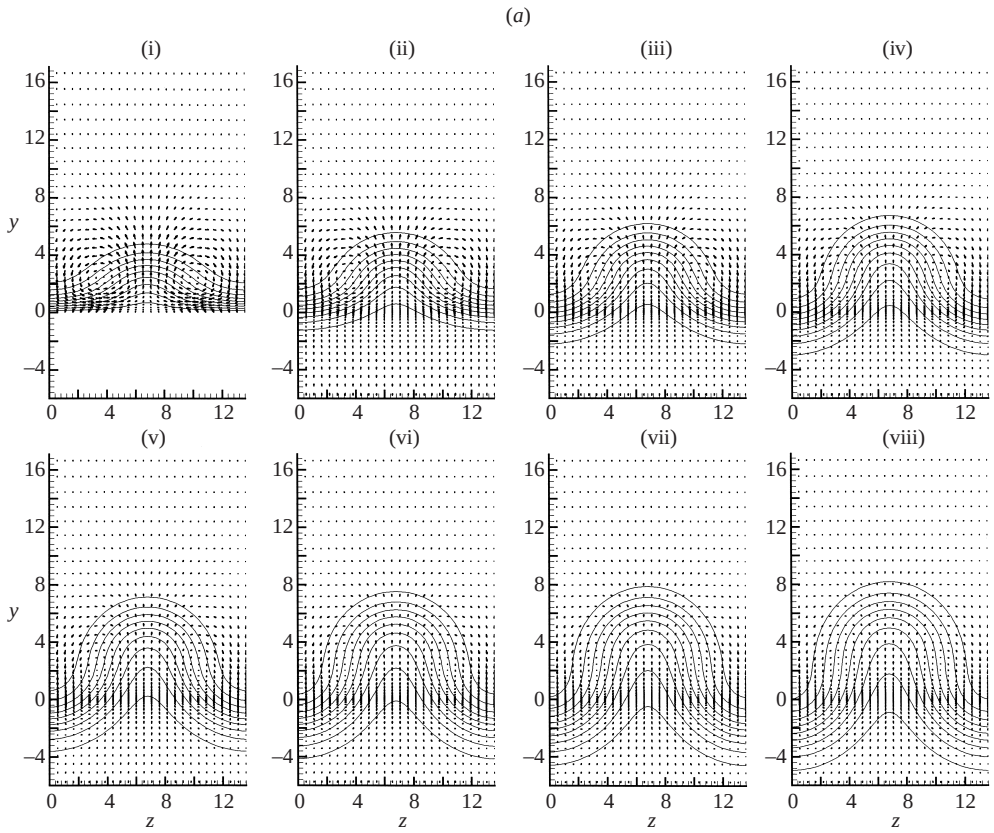

FIGURE 2 (*a*). For caption see facing page.

tional starting position for initiating the weak Görtler vortex at $\delta_0 = (\nu X_0/U_0)^{1/2} = 0.13\,\text{cm}$ or $X_0 = 60\,\text{cm}$ from the leading edge, for which $u'_{max} = 0.12U_0$. These values lead to the dimensionless parameters used in the analysis: the Taylor–Görtler number $G = (U_0\delta_0/\nu)(\delta_0/R)^{1/2} = 9.22$, wavenumber $\beta = 0.46$, spatial amplification rate $\sigma = 3.59$ and the wavelength parameter, which is invariant to the definition of the Taylor–Görtler number used, $\Lambda_\lambda = Re_\lambda(\lambda/R)^{1/2} = 462$ (the λ used in this equation is dimensional). Experimental correlations are generally made in terms of the momentum thickness; the corresponding values in this context are $G_{\theta_0} = (U_0\theta_0/\nu)(\theta_0/R)^{1/2} = 4.99$ and $\beta_{\theta_0} = 0.31$. Concerning the starting conditions on the wall at a given X_0 (or δ_0), note that Lee & Liu (1992) showed quantitatively that the downstream nonlinear development of longitudinal vortices is insensitive to X_0 provided that the local linear instability theory for Görtler vortices is followed with X_0, for a fixed Λ_λ, in describing the initial conditions. The 'spirit' of these initial conditions has been demonstrated in other works as well (Liu & Domaradzki 1993; Park & Huerre 1995; Sabry & Liu 1988, 1991; Benmalek & Saric 1993).

3.1. *The flow structure*

The distance along the wall in which the longitudinal vortices are allowed to develop becomes an important parameter in the subsequent search for optimal enhanced mixing in the downstream region behind the trailing-edge cutoff. Although Lee & Liu (1992) showed that the nonlinear development of Görtler vortices is independent

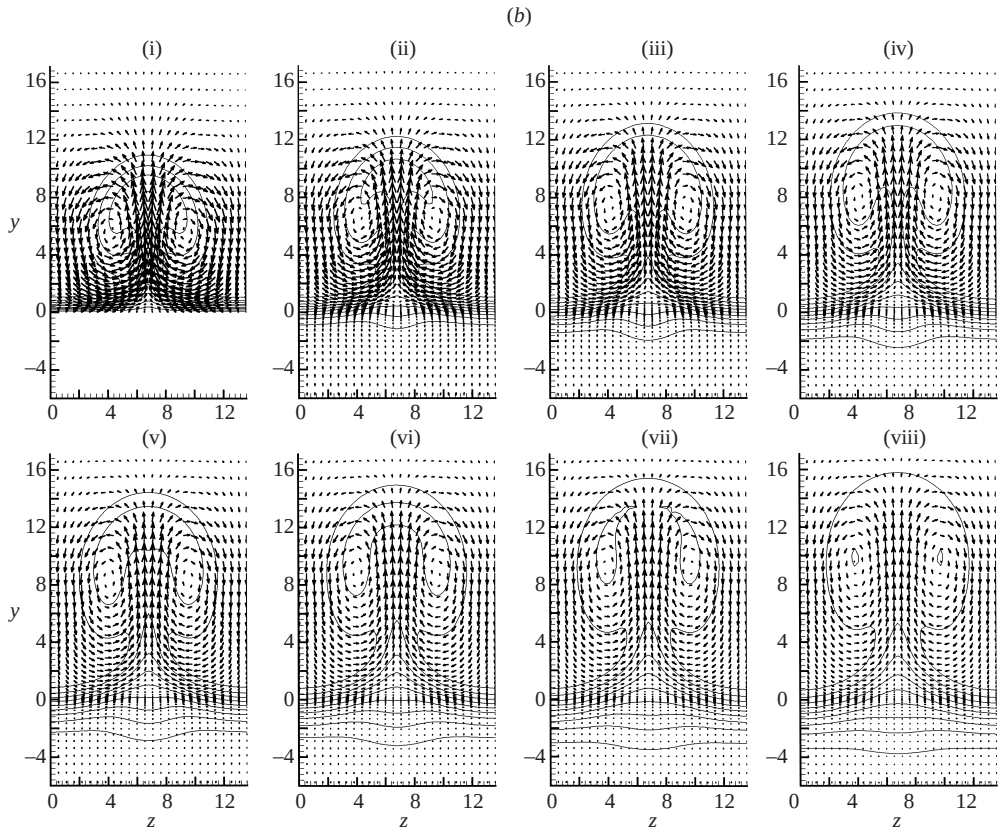

FIGURE 2. Downstream development of iso-u contours and the v, w-vector field in cross-sectional planes for different trailing-edge lengths: (*a*) $X_g = 70$ cm, (*b*) $X_g = 110$ cm. (i) $X = 0$ cm (IC), (ii) 10 cm, (iii) 20 cm, (iv) 30 cm, (v) 40 cm, (vi) 50 cm, (vii) 60 cm, (viii) 70 cm.

of X_0, in order to be consistent with the scale analysis used, the distance along the wall from the leading edge to its cutoff at the trailing edge is denoted by the new dimensionless parameter $x_g = X_g/X_0$.

In the mixing region, the origin of the dimensionless streamwise coordinate begins at the trailing edge at x_g (i.e. $x_{\text{mixing region}} = x_{\text{wall region}} - x_g$), where the wall-bounded nonlinear flow position at the trailing edge is now denoted by $x = 0$. In presenting the results we use the dimensional X, to be consistent with the prevailing practice in the experimental literature (e.g. Swearingen & Blackwelder 1987).

In the initial study, the ambient velocity depicted in the lower stream (the 'secondary flow' in mixing terminology) is taken to be zero. Figures 2(*a*) and 2(*b*), for trailing-edge lengths $X_g = 70$ cm and 110 cm, respectively, show detailed pictures of the total iso-u velocity contours in the (y, z) cross-sectional planes superimposed on the cross-sectional velocity (v, w) vector field. The initial condition at $X = 0$ shows different nonlinear stages of the wall-bounded longitudinal vortices as they develop up to their respective X_g. The wall is located at $y = 0$; the extent of the spanwise region is measured by z, for which the half-wavelength location is $\lambda/2\delta_0 = 6.82$. Unconstrained by the wall in the mixing region, v velocities in the upwash region, at the centre of the (y, z)-plane now advect low-momentum fluid upwards into the high-velocity regions, whereas in the downwash regions on the left and right sides of the (y, z)-plane the

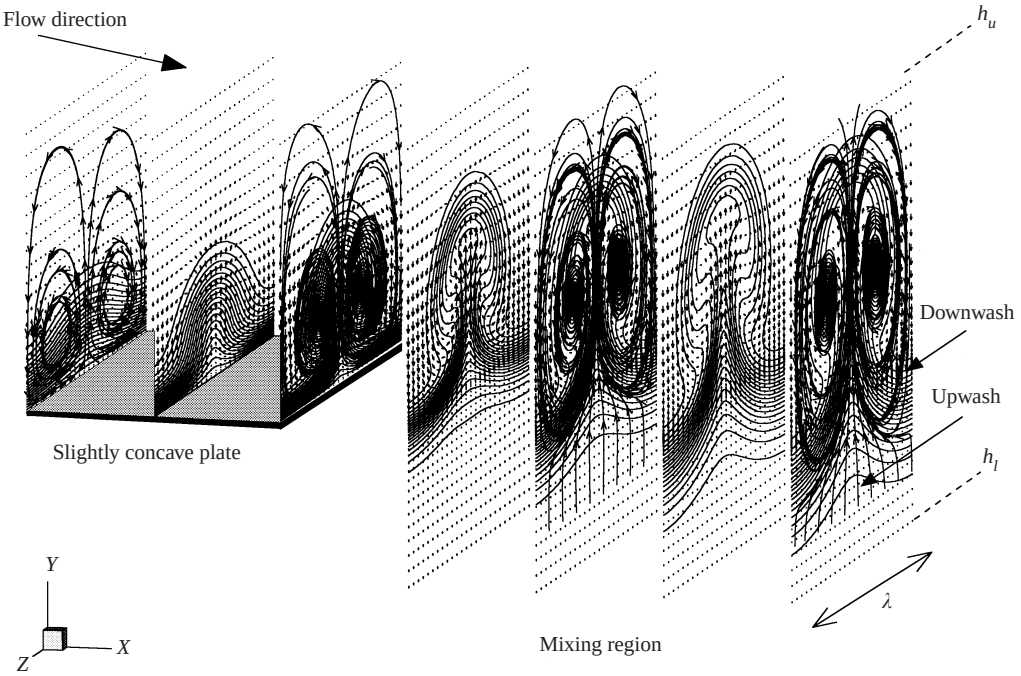

FIGURE 3. Nonlinear development of longitudinal vortices in the mixing region, $X_g = 90\,\text{cm}$.

downward v velocities advect high-momentum fluid into the low-velocity region, as shown in figure 3 (where cross-sectional psuedo-streamlines connect cross-sectional velocity vectors to illustrate the counter-rotating vorticity elements).

As expected, the distance X_g over which the longitudinal vortices develop on the wall before being released into the free mixing region is an important parameter for mixing enhancement. For $X_g = 70\,\text{cm}$, the downwash region lowers the high-speed-fluid iso-u contours into the low-speed region, but the associated upwash and downwash vectors are small relative to the $X_g = 110\,\text{cm}$ case. On the other hand, while the upwash and downwash vectors are relatively larger for the $X_g = 110\,\text{cm}$ case, the high-speed regions of the iso-u contours do not appear to lower into the low-speed fluid. Additional calculations for 80 cm, 90 cm and 100 cm reflect this same qualitative behaviour and mushroom shapes were also obtained.

Visually, the $X_g = 90\,\text{cm}$ case (see figure 3) appears to promote better mixing. The interpretation of iso-u contours in terms of iso-concentration and iso-thermal contours for $Sc = Pr = 1$ is immediate from the discussion of scalar transport in § 2.3.

3.2. *Spanwise-averaged flow field*

The Reynolds-averaged mean velocity in the present problem is the spanwise-averaged profile $\bar{u}(x, y)$. These inflectional profiles develop in the wall region, owing to the upwards advection of low-momentum fluid, and persist well into the free-mixing region; this is more apparent for larger values of X_g where the momentum advection by the longitudinal vortices can develop further along the wall prior to release into the mixing region. The spanwise-averaged velocity profiles are not of particular interest as they are the result of the two-dimensionalization of a real three-dimensional problem. The secondary instabilities are associated with the three-dimensional steady inflectional profiles and will be addressed more fully in §§ 4 and 5 in connection with

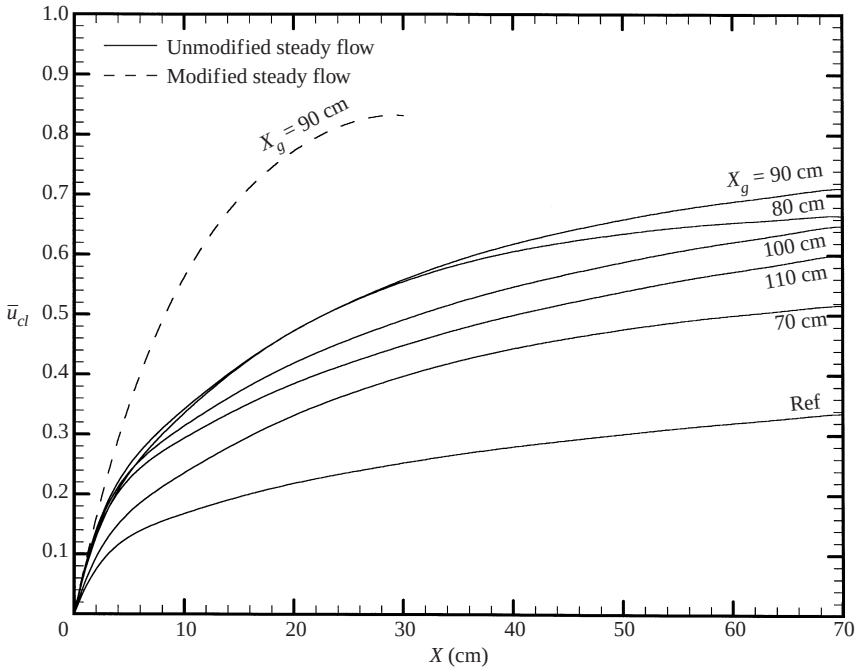

FIGURE 4. Mean centreline velocity $\bar{u}_{cl}(x)$ development.

the three-dimensional profiles $u(y, z; x)$ rather than the spanwise averaged profiles $\bar{u}(x, y)$. What is of interest here is the centreline value of $\bar{u}(x, y)$, which is denoted by $\bar{u}_{cl}(x)$. In laminar mixing, the centreline velocity approaches the asymptotic value $\bar{u}_{cl}(\infty) \to 0.587$ for a velocity ratio of $U_1/U_0 = 0$ ($\bar{u}_{cl}(\infty) \to 0.765$ for $U_1/U_0 = 0.5$), according to the similarity solution far downstream without longitudinal vortices. The streamwise rapidity with which $\bar{u}_{cl}(x)$ equilibrates towards the far-downstream value indicates enhanced mixing. However, because of the distorted mean velocity profiles in the presence of longitudinal vortices, it is questionable to rely on $\bar{u}_{cl}(x)$ alone to indicate the extent of mixing enhancement. The development of $\bar{u}_{cl}(x)$ is shown in figure 4 with X_g as the parameter; included for comparison is the reference case in the absence of longitudinal vortices. Both the $X_g = 80$ cm and 90 cm cases are slightly more vigorous in accelerating the equilibration of $\bar{u}_{cl}(x)$ than the other cases shown for small distances from the trailing edge; eventually the 90 cm case is the most vigorous and $X_g = 70$ cm is the least vigorous. Beyond what is shown in figure 4, no attempt has been made here to study the asymptotic approaches far downstream. Mixing enhancement in applications is expected to be achieved well upstream in the developing non-equilibrium region. Any equilibration towards the similarity solution is not of significant interest for the desired mixing enhancement over short distances.

3.3. *Mass flow and entrainment*

An estimate of the local (in x) net mass entrained into the mixing layer is obtained by integrating the continuity equation over the region $(x - x_g, \Delta h, \lambda)$, where $\Delta h = h_u - h_l$; the limits of integration are well beyond the edges of the shear layer $h_u \gg \delta_u$, $h_l \gg \delta_l$ (see figure 3) and are thus independent of x. The integration across the spanwise region over one wavelength sums over all the explicit effects due to longitudinal vortices. Because the spanwise velocity is periodic, there is no net spanwise mass flow

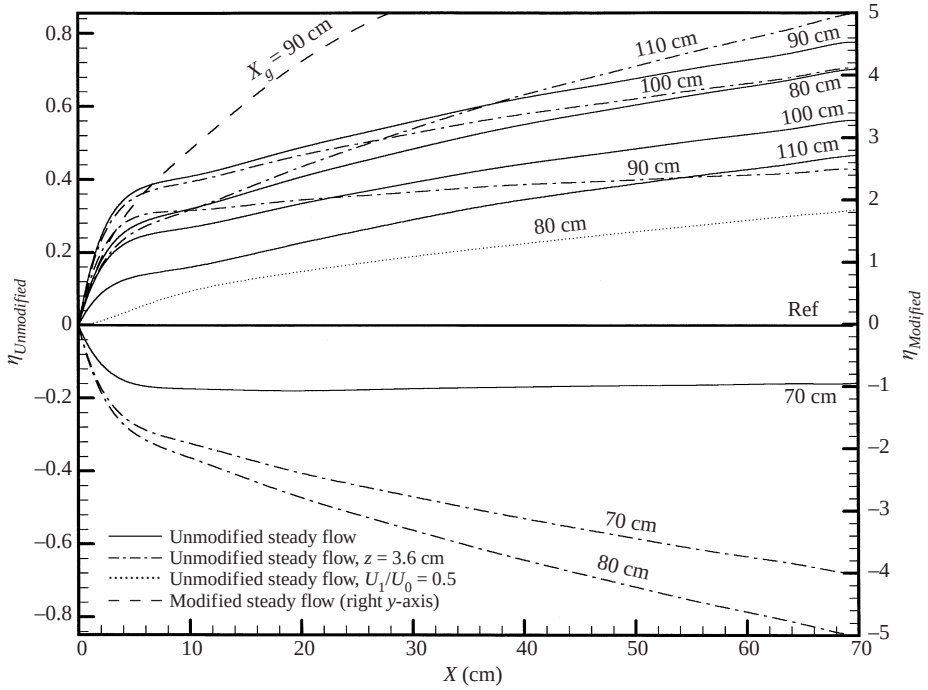

FIGURE 5. Mixing efficiency development.

across the wavelength. In this case, the net dimensionless mass entrained is

$$\lambda\rho\int_{-h_l}^{h_u}\bar{u}(x,y)\,\mathrm{d}y-\lambda\rho\int_{-h_l}^{h_u}\bar{u}(x_g,y)\,\mathrm{d}y=\lambda\rho\int_{x_g}^{x}[\bar{v}(h_l,x)-\bar{v}(h_u,x)]\,\mathrm{d}x\equiv\dot{m}, \tag{3.1}$$

where ρ (constant) is the dimensionless fluid density (which is unity) and is brought in to give the dimensionless equation a more physical appearance. Equation (3.1) has the simple control-volume interpretation that the net mass entrained (denoted by $\dot{m}$), across the planar regions $x-x_g$, λ at $h_u \gg \delta_u$ and $h_l \gg \delta_l$ is equivalent to the net mass flow due to the streamwise velocity over the cross-sections Δh, λ at x and x_g. On the basis of entrainment, the mixing efficiency parameter (described, for instance, by Carletti & Rogers (1995) for a cylindrical ejector) is here defined as

$$\eta=(\dot{m}/\dot{m}_{ref})-1, \tag{3.2}$$

where $\dot{m}_{ref}$ is the corresponding net mass entrained in the reference case in the absence of longitudinal vorticity elements on the wall and in the mixing region. The numerical expression for η is then simply

$$\eta=\left[\int_{-h_l}^{h_u}\bar{u}(x,y)\,\mathrm{d}y-\int_{-h_l}^{h_u}\bar{u}(x_g,y)\,\mathrm{d}y\right]\Bigg/\left[\int_{-h_l}^{h_u}\bar{u}(x,y)\,\mathrm{d}y-\int_{-h_l}^{h_u}\bar{u}(x_g,y)\,\mathrm{d}y\right]_{ref}-1. \tag{3.3}$$

The mixing efficiency η is shown in figure 5, with X_g as a parameter. The $X_g = 70\,\mathrm{cm}$ case falls slightly below zero, indicating a slight reversal in entrainment. For other values of X_g indicated, η is positive, with the $X_g = 90\,\mathrm{cm}$ case being optimal among the numerical examples calculated (as anticipated in § 3.1) and $\eta \approx 80\%$ at the end of

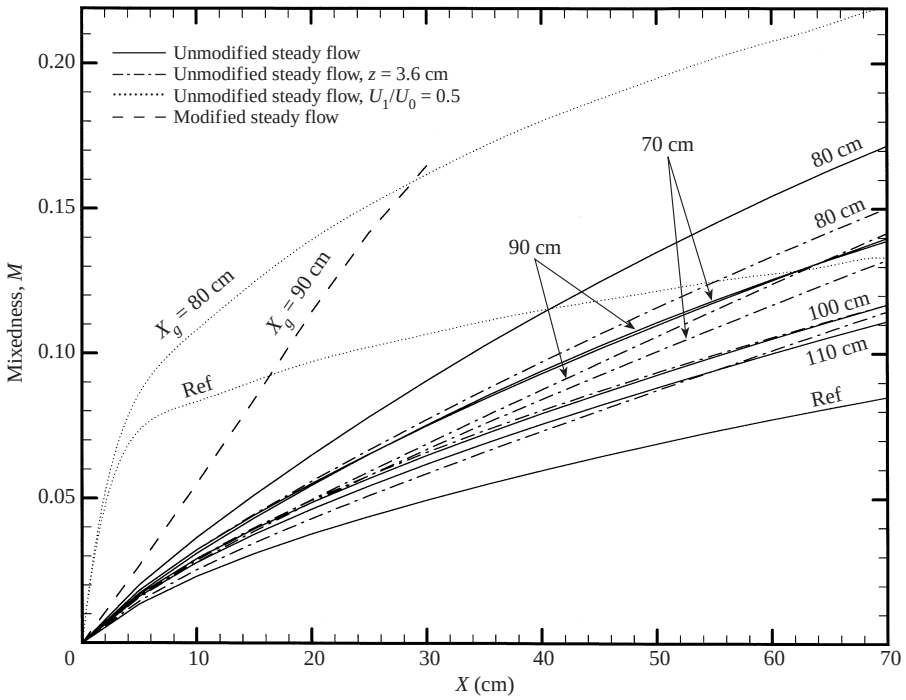

FIGURE 6. Mixedness development.

a mixing region length of $X = 70\,\text{cm}$ or 39 equivalent spanwise wavelengths behind the trailing edge.

3.4. *Mixedness*

In order to assess mixing efficiency from different points of view, we introduce the mixedness parameter, based on the variance of an advected scalar quantity. The dimensionless temperature θ is related to the total streamwise velocity u in the context discussed in § 2.3 for $Pr = Sc = 1$ (Liu & Sabry 1991). If we use standard notation and denote the advected scalar quantity by φ, then in the present case, $\varphi = \theta = u$; the variance σ_v is defined as

$$\sigma_v = \int |u - \hat{u}|\, \mathrm{d}A / \hat{u} \int \mathrm{d}A, \tag{3.4}$$

where $\hat{u}$ is the average of u over the integration $\mathrm{d}A = \mathrm{d}y\,\mathrm{d}z$ carried over the finite cross-sectional region $h_u - h_l$ and λ, which is discussed in § 3.3 and depicted in figure 3. The mixedness parameter M is then defined as

$$M = (\sigma_{v_0} - \sigma_v)/\sigma_v, \tag{3.5}$$

where σ_{v_0} is the variance at the trailing edge. Such a parameter was used, for instance, by Tsui & Wu (1996) in their study of multi-lobe mixers. Figure 6 shows the development of M as a function of the downstream distance; the case denoted Ref is the situation in the absence of longitudinal vortices, where mixedness develops by viscosity alone. It appears that the $X_g = 80\,\text{cm}$ case gives the optimum mixedness.

It seems clear here that, as for the entrainment considerations, the larger X_g case, allowed longitudinal vorticity elements to develop further along the wall, and thus

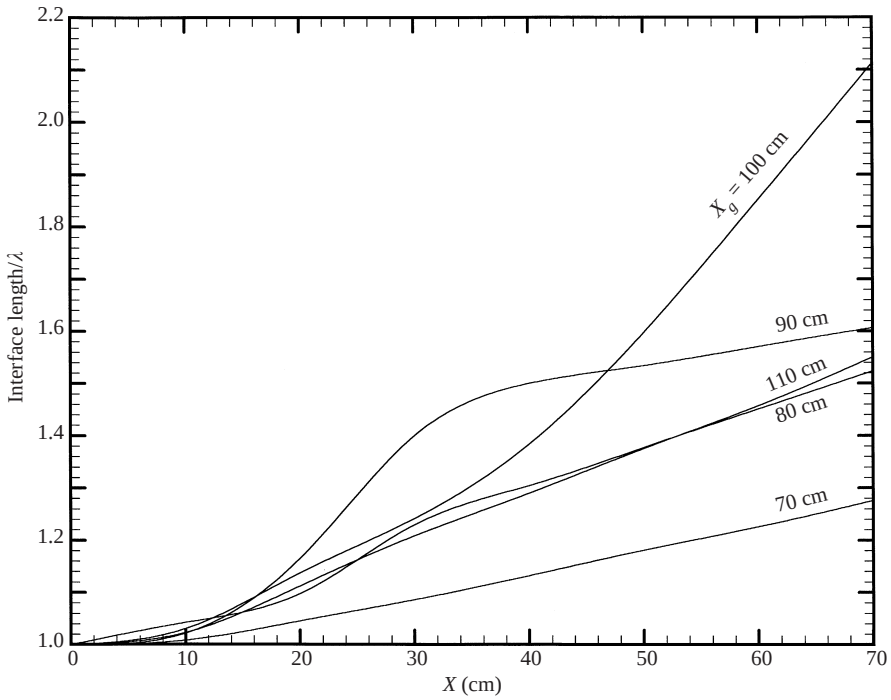

FIGURE 7. Stretching of interface length in the mixing region.

the vorticity elements rose higher above the original interface, thereby lessening their influence on the lower region. At the same downstream region of $X = 70$ cm in figure 6, the mixedness parameter for the optimum $X_g = 80$ cm is about twice (104%) that of the Ref case.

3.5. *Interface stretching and combustion problems*

A lobed-trailing-edge splitter plate has been used in studies of combustion in a mixing-region geometry (McVey 1998; Waitz & Underwood 1996). McVey (1998) showed that, because of enhanced mixing and increased flame speed, the flame spread angle doubled over that for a flat-plate trailing edge. Waitz & Underwood (1996) found that mixing enhancement in the lobed-trailing-edge case was less sensitive to the stabilizing effect of heat release than in the two-dimensional case in the absence of longitudinal vortices.

Lobed fuel injectors have been studied recently for controlling the sequence of mixing and combustion (Mitchell *et al.* 1996; Smith *et al.* 1997). Fuel is injected directly into the longitudinal vortex flow field, where the flow has the largest streamwise vorticity and highest strain rates. Because of the latter, ignition is delayed; because of the high vorticity, fuel and oxidizer are mixed rapidly. Thus it is possible to bring about a mixed or partially mixed fuel–oxidizer system before ignition, thereby reducing pollutants by avoiding ignition under diffusion flame conditions. Mitchell *et al.* (1997) contrasted the characteristics of lobed and non-lobed injectors and found that the visible flame shows a considerable degree of entrained air and premixing so that at least partially mixed, lean flames can be achieved.

The contortion and stretching in the initial interface between two streams as the flow develops downstream is an effective measure of mixing enhancement (see Waitz

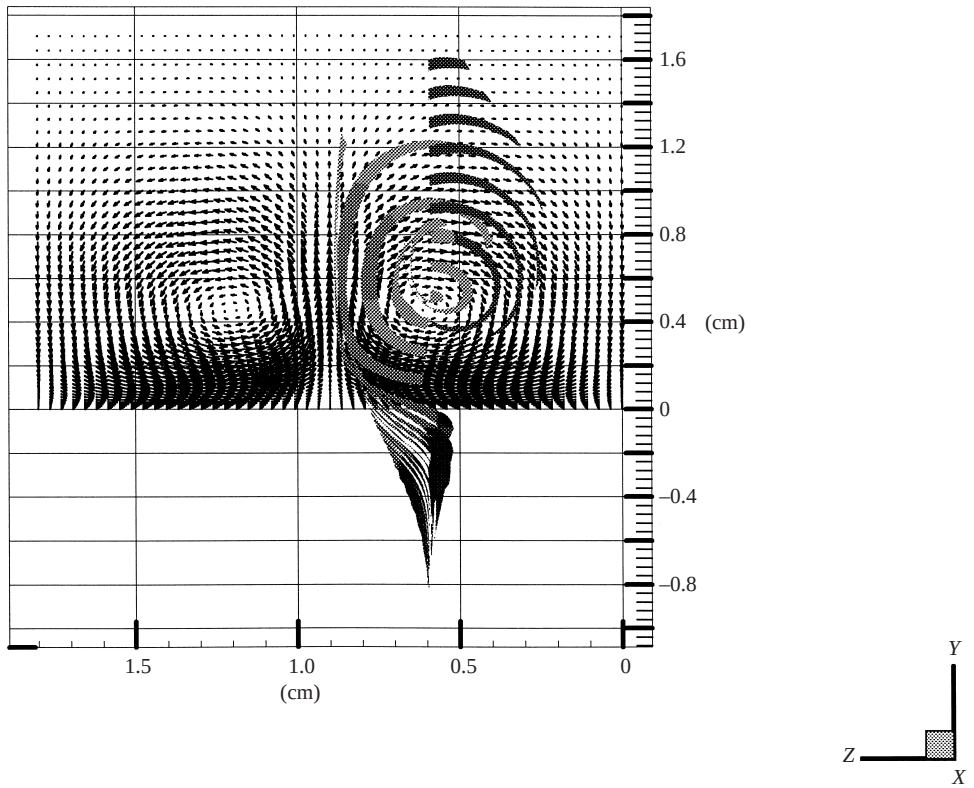

FIGURE 8. Particle paths in the optimal mixing region, with particles released along a vertical line through the centre of the clockwise-rotating longitudinal vorticity element, viewed in the (Y, Z)-plane.

et al. 1997). Particularly important in diffusion-dominated combustion problems, such as non-premixed flames, is the use of large-scale longitudinal vorticity elements to control the extent of combustion via the control of interface surface area available for scalar diffusion towards the interface and hence the extent of reaction at the interface.

In the present problem, the initial interface length separating the two fluids is one spanwise wavelength. The downstream development of the interface stretching by the cross-stream advective velocities of the longitudinal votricity is shown in figure 7. The longer-trailing-edge case, $X_g = 100\,\text{cm}$, produces greater interface stretching further downstream, whereas the $X_g = 90\,\text{cm}$ case produces greater interface stretching closer to the trailing edge.

3.6. *Particle paths*

Tracking particle paths in a given flow field is useful in depicting the mixing mechanism and flow structure (e.g. Yarin *et al.* 1996). To illustrate this, the flow field of the 'optimal mixedness' case (figure 6), $X_g = 80\,\text{cm}$, is used to construct the particle paths in figure 8. Particles are released along a vertical line located at the centre of the clockwise 'vortex' when viewed upstream (to the right of the iso-streamwise velocity mushroom structure), and show the interweaving and twisting of the stream ribbons. Figure 8 also shows the large-scale 'stirring' on the clockwise-rotating side of the vortex as low-momentum fluid is advected upwards into the high-velocity regions.

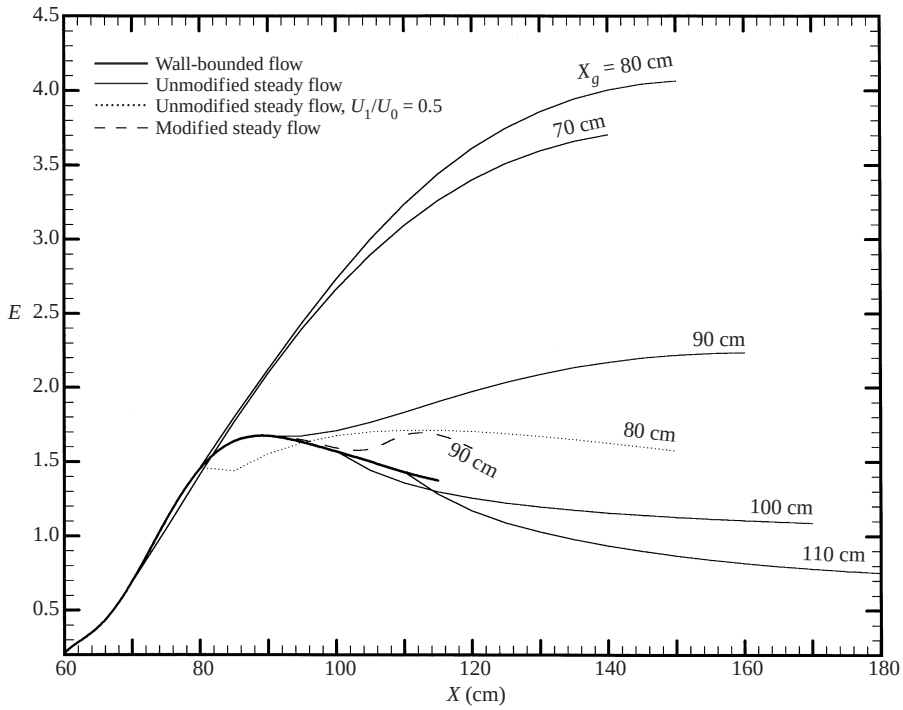

FIGURE 9. Global disturbance energy development along the wall and in the mixing region for various trailing-edge lengths, X_g.

3.7. *Disturbance energy*

The longitudinal vortices released into the mixing region originate from spatially amplified disturbances in the upstream wall region. It is therefore of interest to depict the evolution of disturbance energy in the mixing region. Taking into account the scaling discussed in § 2, the dimensionless total (or global) disturbance energy, referred to free-stream values, is

$$E = \frac{1}{2}\int_{-\infty}^{\infty}\frac{1}{\lambda}\int_{0}^{\lambda}(u'^2 + v'^2/Re_{X_0} + w'^2/Re_{X_0})\,\mathrm{d}z\,\mathrm{d}y, \tag{3.6}$$

for the mixing region. In the wall region, the lower limit in the y integration is zero. The disturbance energy for the wall-bounded flow, shown as the bold-solid line in figure 9, is similar to that obtained earlier in computations (Sabry & Liu 1991; Lee & Liu 1992) and in measurements (Swearingen & Blackwelder 1987) for the steady disturbance component, showing that E amplifies initially and subsequently decays. The solid lines are the mixing-region disturbance energy corresponding to the trailing-edge lengths for the X_g indicated. For the longer lengths $X_g = 100\,\mathrm{cm}$ and 110 cm, where the wall-bounded flow E decays, the disturbance energy in the mixing region also decays.

The $X_g = 90\,\mathrm{cm}$ case corresponds approximately to the maximum disturbance energy for the wall-bounded flow at this trailing-edge cutoff position. For this case, the disturbance energy in the mixing region subsequently amplifies.

For the early stages of cutoff for the longitudinal vortices, the $X_g = 70$ and 80 cm cases, the disturbance energy is considerably amplified in the mixing region. However, as assessed earlier, these two cases were not those for which the mixing efficiency

(figure 5) or the interface stretching (figure 7) is optimal. However, the $X_g = 80\,\text{cm}$ case provides an optimal mixedness parameter for the flow field (figure 6).

In the present spatial problem, it is the global mean advection of disturbance energy that is subject to 'amplification' rather than the global disturbance energy alone, as in the temporal problem. The advected global disturbance energy balance in the mixing region is obtained using the simplified parabolic partial differential equations (e.g. Lee & Liu 1992) to form the mean spanwise-averaged kinetic energy equation, subjected to integration across the shear flow. The resulting integrals describing energy advection, exchanges and conversions are evaluated by inserting the computed results into the integrand. This technique is very similar to that discussed in detail for the steady wall-bounded flows (Lee & Liu 1992) and the details are thus described only briefly.

In the mixing region, the flow is taken as tangential to the trailing edge, so that the centrifugal mechanism does not appear in the energy balance. It is necessary, however, to point out an anomaly for wall-bounded flow that arises from the commonly accepted scale analysis performed on the momentum equations when only the Görtler centrifugal instability mechanism Gu^2 is retained in the y-momentum equation. This analysis neglects the mechanism $-Guv$ in the x-momentum equation, which was retained by Hämmerlin (1955). As noted by Sabry & Liu (1991), the Görtler mechanism alone produces an apparent energy source Gvu^2 for the kinetic energy contribution $v^2/2$, but this must not be taken literally as a net source of energy in the global energy balance. This is because the Hämmerlin mechanism, though 'small' in the momentum sense in the scale analysis, produces an equal and opposite energy exchange mechanism in the $u^2/2$ kinetic energy contribution. In the global kinetic energy balance, therefore, the exchanges between $u^2/2$ and $v^2/2$ due to centrifugal instabilities are cancelled. This cancellation holds independently of our assumption of tangential flow off the trailing edge.

The global disturbance (kinetic) energy balance in the mixing region is thus stated as

$$\frac{\mathrm{d}}{\mathrm{d}x}(\text{mean advection of energy}) = \text{Production} - \text{Dissipation} - \frac{\mathrm{d}}{\mathrm{d}x}(\text{'eddy' diffusion}). \tag{3.7}$$

The streamwise rate of change of mean flow advection of disturbance energy is brought about by the balance among disturbance energy production from the spanwise averaged mean flow, the rate of viscous dissipation and the streamwise 'eddy' diffusion through the triple correlations. The global disturbance energy consists mainly of contributions from the streamwise disturbance kinetic energy. Thus the global mean advection of disturbance energy is provided predominantly by the streamwise velocity component, as would be expected from the scaling in § 2. (However, in the differential equation computation, all three-dimensional velocity components must be computed according to § 2.) The disturbance energy comes mainly from the streamwise component of the kinetic energy $u^2/2$.

We studied a few cases for illustration purposes and found that, for $X_g = 90\,\text{cm}$ and 80 cm at least, the production from the Reynolds shear stress working against the mean shear rate of strain is positive,

$$\int_{-\infty}^{\infty} -\overline{u'v'}\,\frac{\partial \bar{u}}{\partial y}\,\mathrm{d}y > 0,$$

reflecting a positive energy flow to the disturbance from the mean flow. The Reynolds

normal stress conversion mechanism is negative,

$$\int_{-\infty}^{\infty} -\overline{u'^2}\,\frac{\partial \bar{u}}{\partial x}\,\mathrm{d}y < 0,$$

reflecting an energy flow from the disturbance back to the mean flow. However, as shown by the scale analysis, the Reynolds shear stress conversion mechanism dominates. The production mechanism, though decreasing from the trailing edge, has a relatively large value at the trailing edge that initially offsets dissipation, so that the rate of advected energy increases. The dominant contribution to the rate of viscous dissipation comes from the dissipation of the streamwise component of the kinetic energy. Because the scaled problem is parabolic, the dissipation is predominantly that in the (y, z)-plane,

$$\int_{-\infty}^{\infty} \left[\overline{\left(\frac{\partial u'}{\partial}\right)^2} + \overline{\left(\frac{\partial u'}{\partial x}\right)^2} \right] \mathrm{d}y.$$

'Eddy' diffusion through the triple correlations plays a minor role in the energy balance.

3.8. *Spanwise spectral content*

The longitudinal vorticity elements sent into the mixing region are initiated upstream in the wall region at a given wavelength. It is known that in wall-bounded flows (e.g. Swearingen & Blackwelder 1987; Tani 1962) the initiated Görtler vortices persist downstream with the same initial physical wavelength for a given set of experimental conditions so that the wavelength parameter Λ_λ remains constant. In order to assess the spectral content of both the wall-bounded and mixing-region flows from the present theoretical and computational results more simply, the disturbance streamwise velocity component is first integrated across the shear flow so that the y-dependence is removed. This 'signal' is then subjected to a Fourier transform:

$$f(n; x) = (2\pi)^{-1/2} \int_0^{2\pi} \exp(-\mathrm{i}nz) \int_{-\infty}^{\infty} u'(x, y, z)\,\mathrm{d}y\,\mathrm{d}z. \tag{3.8}$$

The magnitude of this transform was computed as a function of the mode number n for the mixing region in the case of $X_g = 90\,\mathrm{cm}$ (not shown here). The dominant peak still follows mode number unity with some broadening in the spectrum. This is similar to wall-bounded flows, as pointed out by Saric (1994) in his discussion of Benmalek's computations (Benmalek 1993; Benmalek & Saric 1994).

3.9. *Some effects of initial conditions*

It was crucially recognized in early studies that the development of strongly nonlinear vortices in relatively thin boundary layers is a parabolic problem, with the streamwise distance playing the role of 'time' (Floryan & Saric 1982; Hall 1983). The problem is indeed an upstream-initial-value problem and is thus susceptible to control even in a passive sense. Sabry & Liu (1991), Liu & Sabry (1991), Lee & Liu (1992) and Liu & Lee (1995) studied quantitatively the effect of initial conditions on the downstream development of such vortices and their transport effects. It was first clarified (Lee & Liu 1992) that the computational problem must start with the local parameters of the problem and that the starting flow structure must satisfy the hydrodynamical conservation equations (not just the equation of continuity), at least at the level of the local linear Görtler instability (see also Liu & Domaradzki 1993; Benmalek & Saric 1994; Park & Huerre 1995). In this case, the downstream development is not

dependent upon the upstream location (or the initial times in the temporal problem) of the disturbance initiation. In the following the effects of varying the spanwise wavelength and velocity ratio are discussed.

3.9.1. *Spanwise wavelength*

The main computational results for mixing enhancement here use the steady Görtler vortex flow upstream in a parameter range that is known experimentally (e.g. Swearingen & Blackwelder 1987) for its vigorous development in the most amplified region. This is referred to as the standard case. In terms of upstream parameters, it is known that for wall-bounded flow an increase in the spanwise wavelength, while keeping the initial Görtler number fixed, decreases the transport activity of the nonlinear longitudinal vorticity elements (Sabry & Liu 1991; Liu & Sabry 1991). To illustrate the downstream effect on mixing, the wavenumber is halved from $\beta = 0.46$ to $\beta = 0.23$, corresponding to increasing the wavelength parameter Λ_λ from 462 to 1308 (in dimensional form, λ_z is increased from 1.8 cm to 3.6 cm). For the same Görtler number $G = 9.22$, the initial linear amplification rate is then decreased from $\sigma = 3.59$ to 2.43. Thus for the same initial disturbance amplitude $u'_{max} = 0.12U_0$, longitudinal vortices are expected to develop less vigorously than in the initially more amplified case. Consequently, almost all calculated mixedness values for $X_g = 70$ cm, 80 cm and 100 cm are decreased for the same streamwise lengths of the mixing region as for the standard case (shown figure 6); the mixedness level for the $X_g = 90$ cm case remains unchanged, and the $X_g = 110$ cm case has a slight increase. It should be pointed out that in the mixedness calculations the integration in the spanwise direction is consistently performed over the subject wavelength.

We have already seen in figure 5 that the mixing efficiency at $X_g = 70$ cm for the standard case falls below zero, reducing entrainment below the reference value for this case. In the increased wavelength case, the calculated result shows that both $X_g = 70$ cm and 80 cm cases significantly offset the entrainment properties of the basic reference case, to the extent of halting entrainment at the end of the computed mixing region. The entrainment efficiency is significantly decreased for $X_g = 90$ cm, while for $X_g = 100$ cm and 110 cm it is increased.

This latter increase can perhaps be explained from the flow structure at the end of the computed mixing region ($X = 70$ cm), not shown here, in which a secondary downward pointing (negative y-direction) mushroom structure develops that induces further entrainment from the negative-y side, as the connected vectors in the (y, z)-plane indicate. The standard case also shows entrainment from the negative-y side but to a less developed extent, which accounts for the smaller η in figure 5 at the same $X = 70$ cm location.

3.9.2. *Effect of velocity ratio*

The computations for the 'standard case' were performed for zero secondary-stream velocity $U_1 = 0$. To illustrate the effect of a non-zero velocity, computations are performed for $U_1/U_0 = 0.5$ and $X_g = 80$ cm. In contrast to the $U_1/U_0 = 0$ case of figure 2, the secondary stream in the present case initially supports a trailing-edge boundary layer without longitudinal vortices at $x = 0$ and $y < 0$.

Although the mushroom shape of the iso-u structure develops less fully and occupies less area in the (y, z)-plane for the $U_1/U_0 = 0.5$ case, there appears to be more uniformity within the affected regions than the $U_1/U_0 = 0$ case, which accounts for the large mixedness values shown in figure 6: 0.22 compared to 0.17 at the same downstream location, $X = 70$ cm. This is mainly attributable to the smaller

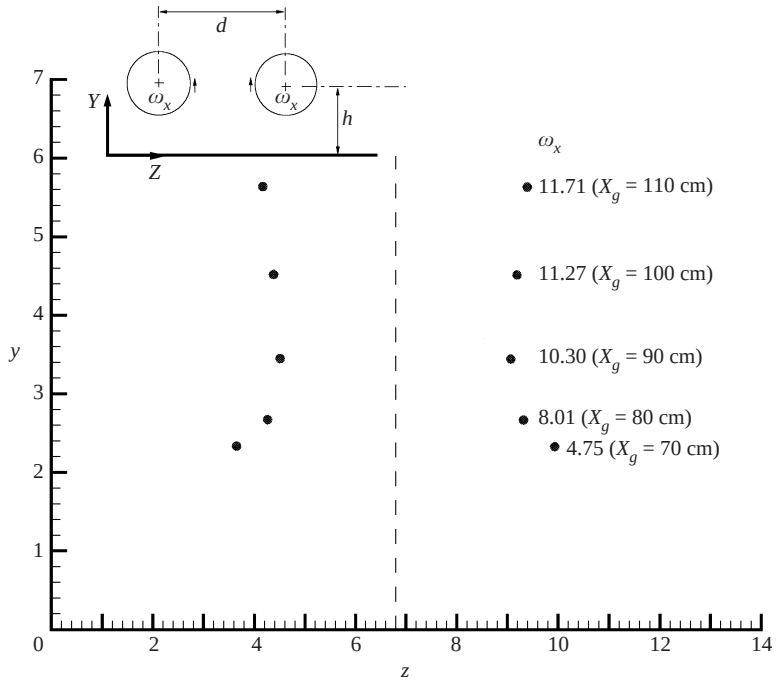

FIGURE 10. Longitudinal 'vortex centre' location and vorticity strength (magnitude of ω_x) for various trailing-edge lengths.

amplification of the longitudinal vorticity elements in the mixing region in the weaker mean shear ($U_1/U_0 = 0.5$) case. These remarks also hold for the scalar problem because of the similarity between iso-u and iso-θ discussed in § 2.3. On the other hand, the mixing efficiency for the $U_1/U_0 = 0.5$ case is approximately half of that for $U_1/U_0 = 0$ at the same downstream location, $X = 70$ cm (see figure 5). The corresponding energy for this case is shown in figure 9, which is weaker that the $U_1/U_0 = 0$ case, again because of the lower amplification rate.

3.10. *Streamwise vorticity centres at the trailing edge*

The dimensionless streamwise vorticity magnitude ω_x at its 'vortex centre', that is, at the centre of the pseudo-two-dimensional streamline pattern in the (y, z)-plane, is depicted in figure 10 at each trailing-edge length X_g for the single-stream mixing-layer case. As discussed in connection with mixing parameters, the optimal X_g is associated not necessarily with the largest ω_x, but instead with modest ω_x and close proximity of the vortex centre to the 'low-velocity' region. The characterization of mixing using the centre values of $\omega_x(X_g)$, or the equivalent circulation of one of the counter-rotating vortices, would not be as useful in the present context as in the case of lobed trailing edges (e.g. Waitz *et al.* 1997). In the lobed-trailing-edge case, as well as when using explicit vortex generators, the streamwise vorticies generated are very nearly mimicked by potential vortices with a viscous or turbulent core (Waitz *et al.* 1997). In this case the strength of the vortices decays downstream through dissipative mechanisms. In the present studies, the vortices sent downstream possess their own Reynolds stresses for amplification (even after the initial centrifugal force has been switched off in the mixing region) and only later succumb to dissipative mechanisms. This again points

to the difference between vortices, which decay after generation, and 'vortices' which are sustained by instability mechanisms as in the present studies.

4. Excitation of secondary instability in the optimal steady longitudinal vorticity elements: discussion and formulation of the problem

Sections 2 and 3 studied mixing enhancement via the release of strongly amplified, steady longitudinal vortices into a mixing region. The steady longitudinal vortices, by the nonlinear development of intense local rates of strain, become susceptible to time-dependent secondary instabilities. Their influence in furthering mixing enhancement is studied in this and the following section. We first present a brief review of secondary instabilities of longitudinal vortices in wall-bounded flows as a basis for studying secondary instabilities in the free-mixing region.

It is known from experimental studies that in wall-bounded flows, longitudinal vortices are susceptible to wavy disturbances, commonly known as secondary instabilities (Aihara 1962; Bippes 1972; Bippes & Görtler 1972; Aihara & Kohama 1981, 1982; Aihara, Tomita & Ito 1985; Ito 1980, 1985, 1988; Swearingen & Blackwelder 1987; see also the reviews by Floryan 1991 and Saric 1994). The strong nonlinear modifications of the flow field by the upwash and downwash activities of the steady longitudinal vortices result in strong local spatial gradients of the dominant total streamwise velocity component that provide sites for shear or secondary instabilities. Swearingen & Blackwelder's (1987) measurements of the secondary instability fluctuations provided a quantitative base for comparisons with theoretical results (e.g. Yu & Liu 1991, 1994; Hall & Horseman 1991, Liu & Domaradzki 1993).

Early work on secondary instabilities of Görtler vortices has been done by Hall & Seddougui (1989) and Bassom & Seddougui (1990) for the large-wavenumber and large-Görtler number limits. The results are not, however, directly applicable to experimental observations where the secondary instability wavelengths are of the order of the local boundary layer thickness and the basic flow is at finite Görtler numbers.

Sabry & Liu (1988, 1991) computed the basic longitudinal vorticity elements developing from initial weak Görtler vortices within the same nonlinear framework of unsteady time-dependent growth of the boundary layer as envisioned by Görtler (1940). Sabry & Liu (1991) mapped out regions of intense $\partial u/\partial y$ and $\partial u/\partial z$ and discussed the sites for secondary instabilities. This was followed by Sabry, Yu & Liu (1990) stability analysis, taking sectional profiles from the full three-dimensional total streamwise velocity profile of Sabry & Liu (1991) as if they were quasi-two-dimensional. Sabry *et al.*'s (1990) results for sections that are most susceptible to secondary instabilities were qualitatively in agreement with the global viscous secondary instability analysis of Yu & Liu (1991). In good agreement with measurements (Swearingen & Blackwelder 1987), Yu & Liu (1991) found that the sinuous mode has the most intense incipient breakdown region in terms of the experimentally comparable contours of the x-component of the secondary instability u'_{rms} close to the wall on both sides of the upwash region, and less intense regions near the shoulders of the mushroom-shaped iso-u contours away from the wall. Other discussions of the wall-bounded-flow secondary instability problem may be found in Hall & Horseman (1991) and Li & Malik (1995), as well as Liu & Domaradzki (1993) and Park & Huerre (1995).

Yu & Liu (1994) showed that the structural features of the two possible modes, varicose and sinuous (drawing upon the similarity with Rayleigh's jet instability when

viewed in the (x, z)-plane of the three-dimensional flow field), follow the dominant production mechanisms of these modes, which in turn trace the dominant velocity gradients of the flow. In this case, the structural features of the varicose and sinuous modes in terms of u'_{rms} indeed follow closely the three-dimensional features of $\partial u/\partial y$ and $\partial u/\partial z$, respectively. Thus in order for the relative intensities of the secondary instability to be correctly located according to observations, the 'mean flow' velocity distribution and its gradients in the analysis must first be computed correctly. Hall & Horseman's (1991) inviscid analysis did not recover the correct structural features for the location of the relative intensities (although the eigenvalues are comparable to those in Yu & Liu (1991) within about 10%, primarily because their computed steady streamwise velocity differed from the experimental profiles (Swearingen & Blackwelder 1987) and from the computed nonlinear steady basic flow used by Yu & Liu (1991)).

Liu & Domaradzki (1993), using the unsimplified full Navier–Stokes equations, carried out direct numerical simulations of Görtler vortices and the nonlinear development of secondary instabilities within the unsteady boundary layer framework. The nature of the 'turbulence', to which the flow eventually evolves was not analysed. It was difficult, in any case, to relate experimentally observed r.m.s. of the time-dependent flow, including secondary instabilities and eventually turbulence (e.g. Swearingen & Blackwelder 1987), to the computed time evolution of spatially period flow. The frequency approximating that of the observed secondary instability, while recovered in linear stability analysis (Yu & Liu 1991), could not be found in the temporal numerical simulations (Liu & Domaradzki 1993). This may be attributed to the pre-selected streamwise wavelength via specification of the streamwise dimension of the computational box size. This simulation confirmed many of the features obtained from the much simpler framework for boundary layer thickness much smaller than the wall radius (Sabry & Liu 1991), as well as results from the linear theory (Yu & Liu 1991, 1994) prior to the development of strong nonlinearities in the secondary instabilities.

Also of interest is the related work of Park & Huerre (1995) on the nonlinear unsteady development of longitudinal vortices in the asymptotic suction boundary layer on a curved surface, which recovered many features of the unsteady boundary layer results (Sabry & Liu 1991; Liu & Domaradzki 1993). Park & Huerre (1995) also performed a linear stability analysis for the secondary instabilities, again obtaining features similar to the secondary instability results for the boundary layer (Yu & Liu 1991, 1994; Liu & Domaradzki 1993). Their u_{rms} structural features differ from those of Hall & Horseman (1991) for reasons already discussed.

Li & Malik (1995) expanded the inviscid linear stability calculations for basic nonlinear longitudinal vortices at spanwise wavelengths that are half and twice that in the detailed experiments of Swearingen & Blackwelder (1987); this work is similar to the variation in computations of basic flow in Sabry & Liu (1991) for other wavelengths and initial conditions. Li & Malik (1995) also obtained the linear solutions for several local downstream locations where the secondary instabilities were observed to have already become nonlinear (Swearingen & Blackwelder 1987). They converted the temporal amplification to a spatial one via the group velocity, a procedure valid only for amplification rates near the neutral point (Gaster 1962). Although observed secondary instabilities occur at relatively large maximum amplification rates, the plot of growth rates (in cm^{-1}) from the linear theory for the varicose (even) and sinuous (odd) modes at different downstream locations (Li & Malik 1995, figure 4) is most instructive. However, caution should be exercised in arguments based only on the

linear theory that do not take into account upstream initial-condition or amplitude effects. In general, Li & Malik's (1995) linear results were consistent with previous analyses (Yu & Liu 1991) for similar parameter ranges.

All linearized secondary stability analyses reported were for the temporal rather than the spatial problem. Yu and Liu attempted the spatial analysis at first but were not successful in obtaining convergence for the problem and thus reverted to the temporal analysis that was reported in Yu & Liu (1991).

Li & Malik (1995) also solved the parabolized nonlinear stability problem, using the 'PSE method' (Herbert 1997) for the observed fundamental spanwise wavelength for the varicose and the sinuous mode, and employing their respective temporal–inviscid linear solutions as upstream initial conditions. The two modes were intermingled at unknown initial relative strengths in the numerical simulations of Liu & Domoradzki (1993), a situation likely to be the case in real flows. It is therefore difficult to attribute dominant energy-conversion mechanisms to one mode or the other, although the linear theory (Yu & Liu 1994) provides a valuable guide to such mechanisms. The nonlinear evolution of secondary instabilities from both the temporal simulation (Liu & Domaradzki 1993) and spatial parabolized computation showed modifications of the familiar initial iso-u_{rms} contours of the secondary instability. The time traces (Li & Malik 1995, figure 11) at a given physical location are more characteristic of the superposition of trigonometric time functions rather than of observed turbulence. Time traces from the temporal simulation (Liu & Domaradzki 1993, figures 10–12) showed the apparent development of higher frequencies; leaving aside the question of whether the development of observed turbulence is within the computational realm (Li & Malik 1995; Liu & Domaradzki 1993) without explicitly accounting for the development of turbulence itself (e.g. Liu 1988). There appears to exist a significant streamwise region in which secondary instabilities exert a strong influence on the mean flow field. It is the role of this influence in mixing enhancement that we study in the following sections.

4.1. *Formulation of the nonlinear secondary instability problem*

The Navier–Stokes temporal simulation of Liu & Domaradzki (1993) encompasses the nonlinear development of secondary instabilities in wall-bounded flow, as already discussed. The nonlinear work of Li & Malik (1995) uses the parabolized stability equations (PSE, e.g. Herbert 1997) in which the streamwise wavenumbers are also unknown but are chosen so that integral norms are satisfied. The normalization used, which is not necessarily unique, follows earlier work (Bertolotti, Herbert & Spalart 1992) and partitions the streamwise development among the shape function, the exponential growth and wave function. As such, it has the effect of making the total kinetic energy of the shape functions of the secondary instability independent of the streamwise development variable; the secondary instability kinetic energy 'amplification' is thus absorbed into the amplification rate in the phase function. The normalization conditions furnish additional relations for the unknown wavenumbers that are to be solved jointly and iteratively with the parabolized stability equations at each streamwise station. The local convergence then allows the forward integration in the streamwise direction to proceed. No such norms are needed for the spanwise wavenumber, which is considered a known input.

Although the PSE method allows the streamwise wavenumber to vary downstream, the development of these wavenumbers was not reported explicitly (Li & Malik 1995). These authors used the inviscid local linear stability results as upstream initial or starting condition for the viscous form of the parabolic stability equations. The

flow structure differs considerably in the linear viscous and inviscid calculations (Yu & Liu 1994) and thus a viscous nonlinear computation using an inviscid upstream structure (Li & Malik 1995) would require an adjustment length that remains to be further elaborated. Their figure 7, showing the instantaneous streamwise velocity plots at a given normal location for both varicose and sinuous modes, suggests that the streamwise wavelength remains 'constant' as the flow evolves downstream.

Swearingen & Blackwelder (1987) reported that the secondary instabilities occurred at about 130 Hz and that this frequency appears to persist until fine-grained turbulence developed. From their figure 3, an instantaneous visualization of the flow field, it appears that the secondary-instability streamwise wavelength of about 2.5 cm also persisted downstream well into the modulated turbulent-flow region. In other visualization pictures (their figure 14), although the streamwise wavelength differs from the original 2.5 cm value, both varicose and sinuous modes have nearly constant wavelengths as they develop downstream.

On the other hand, the eigenvalues provided by the local linear theory appear to predict fairly well the initial characteristics of the observed secondary instabilities. For instance, for the most amplified sinuous mode, the Yu & Liu (1991) viscous analysis predicted a frequency of about 140 Hz for the streamwise wavelength of 2.5 cm (at streamwise station $X = 90$ cm from the leading edge), while Li & Malik obtained 134 Hz for the same wavelength but at $X = 81$ cm (a linear interpolation of their table 1 results). It is more meaningful to make comparisons in terms of the local eigenvalues than at the same X, since the computed local nonlinear steady mean flow differs considerably.

The local linear secondary instability theory is thus seen to provide realistic eigenvalues and the upstream initial flow structure (in the viscous sense), and all indications point to the robustness of the initial streamwise wavelength as the flow develops downstream, similar to the experimentally observed robustness of the spanwise wavelength in the steady vortex development. For the present physical problem, it is thus sensible to circumvent the PSE method and the need to perform iterations around the local eigenvalues and consider them as given by the upstream initial conditions.

In mixing enhancement studies, we consider the excitation of the single most amplified mode of the primary steady longitudinal vortices, which would be the varicose mode. The basic equations are stated and solved in the physical plane below.

4.2. *Basic equations for the nonlinear secondary instability problem*

Beginning with the three-dimensional unsteady Navier–Stokes equations for an incompressible flow in cylindrical coordinates and subsequently converting to wall coordinates, the total flow quantities are split into steady flow and instantaneous disturbance components as follows:

$$Q_t(x, y, z, t) = Q(x, y, z) + Q'(x, y, z, t). \tag{4.1}$$

The steady flow quantities Q include the basic flow and the longitudinal vorticity elements arising nonlinearly from upstream weak Görtler vortices (§§ 2 and 3), whereas the instantaneous disturbances Q' represent the unsteady secondary instabilities only in the absence of turbulence. The spatial variables X, Y and Z are the dimensional streamwise, wall-normal and spanwise coordinates. Unlike the steady flow case, the unsteady disturbances vary in all directions with length scales of the order of the boundary-layer thickness characterized by $\delta_0 = (\nu X_0/U_0)^{1/2}$, where ν is the kinematic viscosity, X_0 is the distance from the leading edge where the initial conditions for the steady part of Görtler vortices are imposed and U_0 is the velocity of the free-stream

flow. As in § 2, we introduce δ_0 and X_0 as convenient length scales but the problem is independent of them (see Lee & Liu 1992). In the numerical application, the same $X_0 = 60\,\text{cm}$ and consequently $\delta_0 = 0.132\,\text{cm}$ are used. The non-dimensional total flow quantities and coordinates, in lower case, are written as

$$x = \frac{X}{\delta_0}, \quad y = \frac{Y}{\delta_0}, \quad z = \frac{Z}{\delta_0}, \quad t = \frac{T U_0}{\delta_0}, \quad u + u' = \frac{U + U'}{U_0},$$
$$v + v' = \frac{V + V'}{U_0}, \quad w + w' = \frac{W + W'}{U_0}, \quad p + p' = \frac{P + P'}{\rho U_0^2}, \tag{4.2}$$

where u, v and w are the x-, y- and z-components of the velocity, t is the time and p the pressure; ρ is here redefined as the physical, rather than dimensionless, (constant) density. Upper-case letters denote the corresponding dimensional quantities. The dimensionless quantities in (4.2) differ from the steady-flow scaling defined earlier: the present scaling 'favours' the nearly isotropic scale of the secondary instability, which is of the order of the boundary-layer thickness. Similar new dimensionless quantities for the steady flow are also defined because of their participation in a simultaneous calculation of the problem. It has been verified that there is no difficulty in retaining the steady flow approximations already obtained.

4.3. *The Reynolds-averaged modified steady flow problem*

Substituting (4.2) into the unsteady Navier–Stokes equations and then averaging in time yields the set of equations satisfied by the steady flow quantities in the Reynolds-averaged form. Parabolization arguments from Floryan & Saric (1982) and Hall (1983, 1988) for viscosity effects are applied to the Reynolds-averaged equations, as in § 2. No empirical assumptions are made about the Reynolds stresses due to secondary instabilities in the steady flow problem, as they are to be obtained from simultaneously calculated nonlinear secondary instability development. As in § 2, it is assumed that the radius of curvature in the longitudinal direction, R, is much larger than the boundary layer thickness, $\delta_0/R = 1/r_c \ll 1$, so that terms of order $\delta_0/R = 1/r_c$ and less are neglected (e.g. Floryan & Saric 1982; Hall 1983). The curvature terms for the divergence of the Reynolds stresses, which originates from advective effects, are also of order $1/r_c$. Consequently, the governing equations for the steady flow can be written as follows:

continuity equation

$$\frac{\partial u}{\partial x} + \frac{\partial v}{\partial y} + \frac{\partial w}{\partial z} = 0, \tag{4.3}$$

x-momentum equation

$$u\frac{\partial u}{\partial x} + v\frac{\partial u}{\partial y} + w\frac{\partial u}{\partial z} = \frac{1}{Re}\left(\frac{\partial^2 u}{\partial y^2} + \frac{\partial^2 u}{\partial z^2}\right) - \left(\frac{\partial \overline{u'^2}}{\partial x} + \frac{\partial \overline{u'v'}}{\partial y} + \frac{\partial \overline{u'w'}}{\partial z}\right), \tag{4.4}$$

y-momentum equation

$$u\frac{\partial v}{\partial x} + v\frac{\partial v}{\partial y} + w\frac{\partial v}{\partial z} + n\frac{u^2}{r_c} = -\frac{\partial p}{\partial y} + \frac{1}{Re}\left(\frac{\partial^2 v}{\partial y^2} + \frac{\partial^2 v}{\partial z^2}\right) - \left(\frac{\partial \overline{v'u'}}{\partial x} + \frac{\partial \overline{v'^2}}{\partial y} + \frac{\partial \overline{v'w'}}{\partial z}\right), \tag{4.5}$$

z-momentum equation:

$$u\frac{\partial w}{\partial x}+v\frac{\partial w}{\partial y}+w\frac{\partial w}{\partial z}=-\frac{\partial p}{\partial z}+\frac{1}{Re}\left(\frac{\partial^2 w}{\partial y^2}+\frac{\partial^2 w}{\partial z^2}\right)-\left(\frac{\partial\overline{w'u'}}{\partial x}+\frac{\partial\overline{w'v'}}{\partial y}+\frac{\partial\overline{w'^2}}{\partial z}\right), \quad (4.6)$$

where Re in the present section is redefined as the Reynolds number based on δ_0, $Re_{\delta_0}=U_0\delta_0/\nu$, where ν is the kinematic viscosity, n is unity on the wall and zero in the mixing region. If we apply the steady-flow boundary-layer scale analysis to the steady Reynolds stress energy-conversion mechanism between the steady flow and the secondary instability, then the Reynolds stress terms that do make a difference are in the x-momentum equation, $-\partial\overline{u'v'}/\partial y-\partial\overline{u'w'}/\partial z$. These are associated with $-\overline{u'v'}\partial u/\partial y$ and $-\overline{u'w'}\partial u/\partial z$ in energy-conversion mechanisms and represent energy flow from the steady flow to the secondary instability if positive and a reverse energy flow if negative. A thorough discussion of the conversion mechanisms is given in Yu & Liu (1994) in connection with the linear problem; those mechanisms are the same in the present simplified nonlinear problem.

The ideas elucidated in discussions of other nonlinear hydrodynamic stability problems (Stuart 1958, 1960, 1962*a*, *b*) have much broader physical consequences that also apply here. Applying those ideas to the present problem, the secondary instabilities here are initiated at small amplitudes, and in the linear region their Reynolds stress effect on the steady flow is negligible. As they amplify by extracting energy from the steady flow in a three-dimensional way, they develop to an extent that nonlinearity becomes important, as manifested in the form of modification of the steady flow, harmonics generation and the modification of their structural features from linear form. In the absence of the Reynolds stresses in the momentum equations (4.4)–(4.6), the system reverts back to that of § 2 for the nonlinear steady flow problem in the absence or presence of linear secondary instabilities.

We point out here again (Sabry & Liu 1991) that in the approximation $\delta_0/R=1/r_c\ll 1$, the surviving centrifugal Görtler instability mechanism due to curvature is nu^2/r_c in (4.5). It plays havoc in an energy balance owing to the absence of the Hämmerlin (1955) mechanism $-nuv/r_c$, which would otherwise contribute to an exchange of kinetic energy between $u^2/2$ and $v^2/2$, and thus nullify the apparent net source nvu^2/r_c for $v^2/2$ itself. However, nu^2/r_c initiates the longitudinal vortices but remains small, in terms of energy, relative to the energy-conversion mechanism of the Reynolds stresses.

The boundary and upstream initial conditions for the steady flow problem are the same as in § 2 and are repeated here for completeness. Periodic boundary conditions are imposed in the spanwise direction. The boundary conditions in the y-direction for the wall region are

$$u=0,\quad v=0,\quad w=0\quad\text{at}\quad y=0, \quad (4.7)$$

$$u\to 1,\quad \partial v/\partial y\to 0,\quad w\to 0\quad\text{as}\quad y\to\infty. \quad (4.8)$$

The boundary conditions in the y-directions for the mixing region are

$$u\to 1,\quad \partial v/\partial y\to 0,\quad w\to 0\quad\text{as}\quad y\to\infty, \quad (4.9)$$

$$u\to U_1/U_0,\quad \partial v/\partial y\to 0,\quad w\to 0\quad\text{as}\quad y\to-\infty. \quad (4.10)$$

4.4. *The nonlinear secondary instability problem*

The secondary instabilities start to develop weakly in the manner predicted by the linear stability theory. At some distance downstream, however, the nonlinearity effects

begin to grow and influence the secondary instabilities in a way that the linear stability theory fails to describe. The nonlinear secondary instability equations, obtained by subtraction of the Reynolds-averaged equations (4.3)–(4.6) for the steady flow from the total flow equations, are written in physical variables in the same spirit as in studies of nonlinear hydrodynamic stability (e.g. Stuart 1956). For $\delta_0/R = 1/r_c \ll 1$, the curvature effects in the continuity equation, as for the steady flow, do not appear:

continuity equation

$$\frac{\partial u'}{\partial x} + \frac{\partial v'}{\partial y} + \frac{\partial w'}{\partial z} = 0. \tag{4.11}$$

In the nonlinear secondary instability momentum equations, for $\delta_0/R = 1/r_c \ll 1$, curvature terms are neglected in the viscous diffusion and advective effects. The latter includes the divergence of the excess 'Reynolds stresses' at the same frequency as the secondary instability, which gives rise to the nonlinear effect of harmonic generation. Neither the centrifugal mechanism of Hammerlin or of Görtler survives this approximation for the secondary instability, as was found by Yu & Liu (1991) and others (Hall & Horseman 1991; Park & Huerre 1995); scaling was not performed in Liu & Domaradzki (1993) and Li & Malik (1995). In addition to simplifications due to $\delta_0/R = 1/r_c \ll 1$, there is also the scaling $Re^{-1} = (U_0\delta_0/\nu)^{-1} \ll 1$ involving the boundary-layer-like steady flow, which plays the dual role of advector of the secondary instability momentum and as a momentum source in terms of steady flow vorticity advected by the secondary instability velocities; only the streamwise advection survives in this approximation. The strongest momentum sources are for the x-momentum in terms of the vertical, or normal, advection of the spanwise steady flow vorticity, which is common and well understood in two-dimensional instability problems (e.g. Lin 1955), and the spanwise advection of the normal component of the steady flow vorticity. Thus the momentum equations have the form

x-momentum equation

$$\frac{\partial u'}{\partial t} + \left(u\frac{\partial u'}{\partial x}\right) + \left(v'\frac{\partial u}{\partial y} + w'\frac{\partial u}{\partial z}\right) = -\frac{\partial p'}{\partial x} + \frac{1}{Re}\left(\frac{\partial^2 u'}{\partial x^2} + \frac{\partial^2 u'}{\partial y^2} + \frac{\partial^2 u'}{\partial z^2}\right) + \left(\frac{\partial\left(\overline{u'^2} - u'^2\right)}{\partial x} + \frac{\partial\left(\overline{u'v'} - u'v'\right)}{\partial y} + \frac{\partial\left(\overline{u'w'} - u'w'\right)}{\partial z}\right), \tag{4.12}$$

y-momentum equation

$$\frac{\partial v'}{\partial t} + \left(u\frac{\partial v'}{\partial x}\right) = -\frac{\partial p'}{\partial y} + \frac{1}{Re}\left(\frac{\partial^2 u'}{\partial x^2} + \frac{\partial^2 u'}{\partial y^2} + \frac{\partial^2 u'}{\partial z^2}\right) + \left(\frac{\partial\left(\overline{u'v'} - u'v'\right)}{\partial x} + \frac{\partial\left(\overline{v'^2} - v'^2\right)}{\partial y} + \frac{\partial\left(\overline{u'w'} - u'w'\right)}{\partial z}\right), \tag{4.13}$$

z-momentum equation

$$\frac{\partial w'}{\partial t} + \left(u\frac{\partial w'}{\partial x}\right) = -\frac{\partial p'}{\partial z} + \frac{1}{Re}\left(\frac{\partial^2 w'}{\partial x^2} + \frac{\partial^2 w'}{\partial y^2} + \frac{\partial^2 w'}{\partial z^2}\right) + \left(\frac{\partial\left(\overline{u'w'} - u'w'\right)}{\partial x} + \frac{\partial\left(\overline{v'w'} - v'w'\right)}{\partial y} + \frac{\partial\left(\overline{w'^2} - w'^2\right)}{\partial z}\right). \tag{4.14}$$

Except for the nonlinear effects, (4.11)–(4.14) are identical to Yu & Liu's (1991) secondary instability equations, Viscosity effects are retained as is necessary to satisfy wall-boundary conditions upstream, without further analysis of the Stokes-like wall layer due to secondary instabilities. As was borne out in Yu & Liu's (1991, 1994) linear analysis, the principal mechanisms for secondary instability are the energy conversion mechanisms from the steady flow, originating from the secondary instability velocity's advection of the respective spanwise and normal components of the steady flow vorticity. Other less important mechanisms can be classified as 'other non-parallel' effects.

As confirmed by many experimental and numerical observations such as Swearingen & Blaclwelder (1987), higher harmonic modes, when present, do not appear to alter the wavelength and frequency of the initiated secondary instability. Moreover, since the Swearingen & Blackwelder experiment indicated a dominant frequency and streamwise wavelength, it seems that the generation of higher harmonics, when present, has no important net effect. The contention here is that the modification of the advecting steady three-dimensional flow by the fundamental mode is more important than effects of cascading into higher harmonics. Thus the present study considers the strong nonlinear effects of the fundamental mode of the secondary instability on the mean flow in absence of the harmonics. This is similar in spirit to the work of Stuart (1958) on plane Poiseuille flow in which the modification of the mean flow by the fundamental was obtained via its Reynolds stresses and the modified mean flow was shown to become more unstable than the unmodified mean flow.

The present work can also be discussed in the light of analysis of the weakly nonlinear theory (Stuart 1960; Watson 1960), transcending the application of this theory to disturbances in plane Poiseuille flow, where all the important nonlinear physical processes are identified in mathematical form. In the weakly nonlinear theory, A_1 is the fundamental amplitude, the harmonic amplitude is A_1^2. Thus the wave envelope of the harmonic is not given inertia of its own, but is determined once the fundamental amplitude is determined. The harmonic is thus sustained by energy transfer from the fundamental component but not from the mean motion. In terms of energy-transfer mechanisms for the fundamental energy, proportional to $|A_1|^2$, the nonlinear effects reside in the Stuart constants $k_1 + k_2 + k_3$ (Stuart 1960), which are coefficients of $|A_1|^4$ in the Stuart–Landau amplitude equation. The physical mechanisms represented by the constants k_1, k_2 and k_3 are, respectively, modification of the mean flow, energy transfer between the fundamental and its harmonic and modification of the fundamental component. In the present problem, the k_1 effects are calculated from the steady flow equations (4.3)–(4.6), which are solved jointly with the k_3 effects (and, in general, the k_2 effects also) from (4.11)–(4.14). The harmonic generation mechanism (k_2 effects) resides in the divergence of the excess local stresses on the right-hand sides of (4.12)–(4.14), and these effects would be absent in the subsequent formulation according to the arguments above on the suppression of harmonics generation. The nonlinear effects enter explicitly in (4.4)–(4.6) through the Reynolds stress effects on the steady flow, but enter only implicitly in the secondary instability equations (4.12)–(4.14) through the modification of advective velocities and the vorticity of the modified steady flow. The numerical procedure is one of 'leap frogging': the initial secondary instability is used in the calculation of the Reynolds stresses; the Reynolds-stress-modified mean flow is then calculated and used to calculate a new secondary instability behaviour in the following step, and so on. Thus each streamwise step is similar in spirit to Stuart (1958).

The wave characteristics of the initiated secondary instability are essentially given by the local linear theory (e.g. Yu & Liu 1991), which is in good agreement with observations; such characteristics appear to be robust in the downstream development (Swearingen & Blackwelder 1987). We reiterate that we bypass the formalism of the PSE (parabolized stability equations) method (Herbert 1997; Li & Malik 1995), which presumes that the local wavenumbers are also unknown but still uses the results of the linear theory to start the computation. The procedure requires auxiliary normalization conditions, which are not necessarily unique, to determine the wavenumbers jointly and iteratively with the solution of the conservation equations as the computation progresses downstream. Although the explicit wavenumbers from such a computation were not presented, the instantaneous streamwise velocity plots at a given wall-normal location in the computed example of Li & Malik (1995) using the PSE method for wall-bounded flow indicate that the wavelengths do indeed remain robust in the streamwise direction for both varicose and sinuous modes.

The question of whether the PSE method does indeed yield 'parabolicity' was addressed in part by Herbert (1997). In the present problem, the coupled conservation equations for the steady flow and the nonlinear secondary instability with given wavelength and frequency have not been studied but appear to be parabolic, given the wavy representation of the secondary-instability flow quantities accompanied by the assumption that the wave envelope varies slowly relative to the waviness.

In order to proceed, we represent the unsteady perturbations in normal-mode form, reflecting the foregoing discussions, with fundamental wave characteristics given by the initial local linear theory:

$$(u', v', w', p') = (\hat{u}, \hat{v}, \hat{w}, \hat{p})\, \mathrm{e}^{\mathrm{i}(\alpha x - \sigma t)} + \text{c.c.}, \tag{4.15}$$

where $\hat{u}$, $\hat{v}$, $\hat{w}$ and $\hat{p}$ are the complex perturbation amplitudes and are functions of (x, y, z). In the streamwise development study, we consider the nonlinear spatial growth of the disturbances. Therefore, α is a complex number, $\alpha = \alpha_r + \mathrm{i}\alpha_i$, that combines the wavenumber $\alpha_r = 2\pi/\lambda_x$ and the spatial amplification rate α_i, λ_x is the disturbance wavelength in the x-direction, and σ is real and represents the disturbance frequency. The normal-mode concept represents the disturbances as rapidly oscillating waves propagating in the streamwise direction, represented by the exponential function in (4.15), which is embedded within slowly varying wave amplitudes or wave envelopes. Thus, the parabolization process here amounts to attributing the dominant streamwise changes of flow quantities to the rapidly varying wavy part and the first derivative of the wave envelope, rather than to the slow variations of the second derivative of the amplitude function. By substituting (4.15) into (4.11)–(4.14), and equating coefficients of the same order, we obtain the parabolic secondary instability equations in spectral form. As we have argued, in the absence of harmonics, the fundamental perturbation complex amplitudes are obtained without the explicit nonlinear effects of the Reynolds stress terms on the right of (4.12)–(4.14). 'Hidden' nonlinearities enter through the modified-mean-flow on the left-hand side of (4.12)–(4.14). For simplicity, the spectral form of the equations is not presented here. These equations are coupled to the steady flow system (4.3)–(4.6) and must be solved simultaneously.

4.5. *Computation of the upstream initial conditions for the secondary instability*

From the observations of Swearingen & Blackwelder (1987) and Tani (1962), Görtler vortices develop downstream following a fixed spanwise wavelength, $\lambda = 2\pi\delta_0/\beta$, where β is the wavenumber in the spanwise direction, even as the boundary layer becomes turbulent (in this study $\lambda = 1.8$ cm and $\beta = 0.461$, as in §§ 2 and 3 above).

Furthermore, according to Swearingen & Blackwelder's (1987) observations, the secondary instabilities have periodic properties in the streamwise direction with streamwise wavelength $\lambda_x = 2.5\,\text{cm}$; this yields a wavenumber $\alpha_r = 0.332$, and constant frequency 130 Hz.

The computation of the spatial nonlinear development of the secondary instabilities starts on the wall, at $X = 90\,\text{cm}$, by using the linear stability profile to approximate the initial conditions. Yu & Liu's (1991, 1994) temporal linear stability analysis is used to obtain the shape of the initial conditions, but they are recomputed here for convenience. The Yu & Liu linear secondary instability equations are a special case of (4.11)–(4.14) in the absence of the nonlinear effects from (i) the divergence of the excess stresses in (4.12)–(4.14) and (ii) modifications of the steady flow velocity by the secondary instability, and are thus independent of the steady flow probem (4.3)–(4.6); the local steady flow velocity is given. After the normal-mode representation, Yu & Liu (1991) considered only a parallel flow and did not retain the x-derivatives of the wave amplitudes. Here we shall consider only the most amplified mode, the sinuous mode, and follow Yu & Liu (1991) in their representation of the sinuous-mode perturbations as follows:

$$(\hat{u}, \hat{v}, \hat{p}) = \sum_{m=0}^{nz} (u_{1m}, v_{1m}, p_{1m}) \sin(m\beta z), \quad \hat{w} = \sum_{m=0}^{nz} w_{1m} \cos(m\beta z), \tag{4.16}$$

where nz is the number of points in the spanwise direction and the subscript 1 represent the sinuous mode in Yu & Liu's notation. The linear stability solution shows that the most amplified sinuous mode has a frequency $\sigma_r = 0.221$; this corresponds to almost 130 Hz, coinciding with the experimental conclusion. It also shows that the temporal amplification rate value is $\sigma_i = 0.043$. The temporal amplification rate arising from the linear stability analysis is related to the spatial amplification rate to be employed to evaluate the spatial growth rate of the secondary instabilities (Gaster 1962). Since in the present problem only a single mode is present, the group velocity is replaced by the phase velocity σ_r/α_r. The spatial amplification rate α_i is obtained from

$$\alpha_i = -(\sigma_i/\sigma_r)\alpha_r.$$

4.6. *Computational procedures*

The numerical computations started with the linear stability problem on the wall at $X = 90\,\text{cm}$, but linear stability results at $X = 85\,\text{cm}$ were also obtained in order to evaluate x-derivatives of the disturbance in starting the numerical solution. The linear stability eigenvalue problem was solved implicitly using a second-order finite difference scheme with a 102×51 non-uniform grid in the (y, z)-plane to cover $50\delta_0$ in the y-direction and one wavelength in the z-direction. The LZ algorithm developed by Kaufman (1975) was employed to compute the complex eigenvalues and eigenvectors for the secondary stabilities.

Subsequently, the Reynolds stresses of the most amplified sinuous mode were computed and utilized to modify the steady flow equations (4.3)–(4.6) at the same streamwise location, $X = 90\,\text{cm}$. The artificial compressibility technique (Chorin 1967) used in §§ 2 and 3 above is also employed here with the same grid arrangement to compute the nonlinear downstream development of the steady flow for the wall-bounded and the mixing regions, taking into consideration the nonlinear effects of secondary instabilities.

The nonlinear spatial downstream development of the sinuous mode of the secondary instabilitiy is then computed at $x + \mathrm{d}x$ using the 'spectral form' of the secondary instability equations. Calculations are performed using implicit second-order finite difference discretization, which is unconditionally stable. The backward Euler scheme is used in the x-direction. The resulting complex linear algebraic equations are solved using the LU factorization technique along with the iterative refinement method to improve accuracy. Subsequently, the steady flow equations are computed at location $x + \mathrm{d}x$. This calculation process continues downstream. In the nonlinear solution of the secondary instabilities, similarly to the leapfrog concept, the steady flow quantities used at location x are modified by the secondary instabilities while the steady flow quantities used at $x + \mathrm{d}x$ are not. The dimensionless value of $\mathrm{d}x$ used was around 0.04. The system of nonlinear partial differential equations was solved in its dimensionless form. In the results, dimensional X is used for easy comparison with the literature.

5. Secondary instability: results and discussion

Here we describe the secondary instability development downstream in the mixing region and assess its role in mixing enhancement. In § 3, it was found that for a set of experiment conditions, optimal mixing enhancement could be achieved by the steady longitudinal vorticity elements through the selection of an optimal trailing-edge length X_{optm}. The most amplified secondary instability and its modification of this particular optimal steady configuration is studied here. It is considered to be forced, imposed at $X_{optm} = 90\,\mathrm{cm}$ and released into the mixing region. Computations are for $U_1 = 0$.

5.1. *Flow structure*

The r.m.s. value of the secondary-instability velocity initial conditions is shown in figure 11(a), and the streamwise velocity component, u'_{rms}, is shown in figure 11(b) for a number of different downstream locations in the mixing region in the (y, z)-plane, where the most amplified linear stability theory solution at $X = 90\,\mathrm{cm}$ on the wall is used as an initial condition profile. The streamwise coordinate, X, is dimensional in the figures and is measured from the trailing edge. As shown in figure 11(b), the initial u'_{rms} at $X = 0$ (for $X_g = 90\,\mathrm{cm}$) coinciding with the results of Swearingen & Blackwelder (1987) and those of Yu & Liu (1991, 1994), possesses two regions with high u'_{rms} values located in the steady flow low-speed region near the wall and on each side of the symmetry line at $Z = \lambda/2$. The u'_{rms} distribution also has two secondary regions with high u'_{rms} values that develop away from the interface line. As the secondary instability amplifies in the mixing region, a third region starts to form on the lower side of the mixing region. The other two velocity components v'_{rms} and w'_{rms} are shown respectively in figures 11(c) and 11(d). The computation of the secondary instability is terminated 30 cm from the trailing edge as its amplitude and energy reach saturation at relatively large values of 12% to 15% of the free-stream velocity values.

Yu & Liu (1994) showed that the structural features of the sinuous mode, similar to Rayleigh's jet instability when viewed in the (x, z)-plane of the three-dimensional flow field, follows the dominant production mechanisms of these modes, which in turn track the dominant velocity gradients or rates of strain of the steady flow. In this case, the structural features of the sinuous mode r.m.s. streamwise velocity closely follow the three-dimensional features of $\partial u/\partial z$, as shown in figure 12, where the streamwise development of $\partial u/\partial z$ and u'_{rms} are compared in their respective (y, z)-planes. The

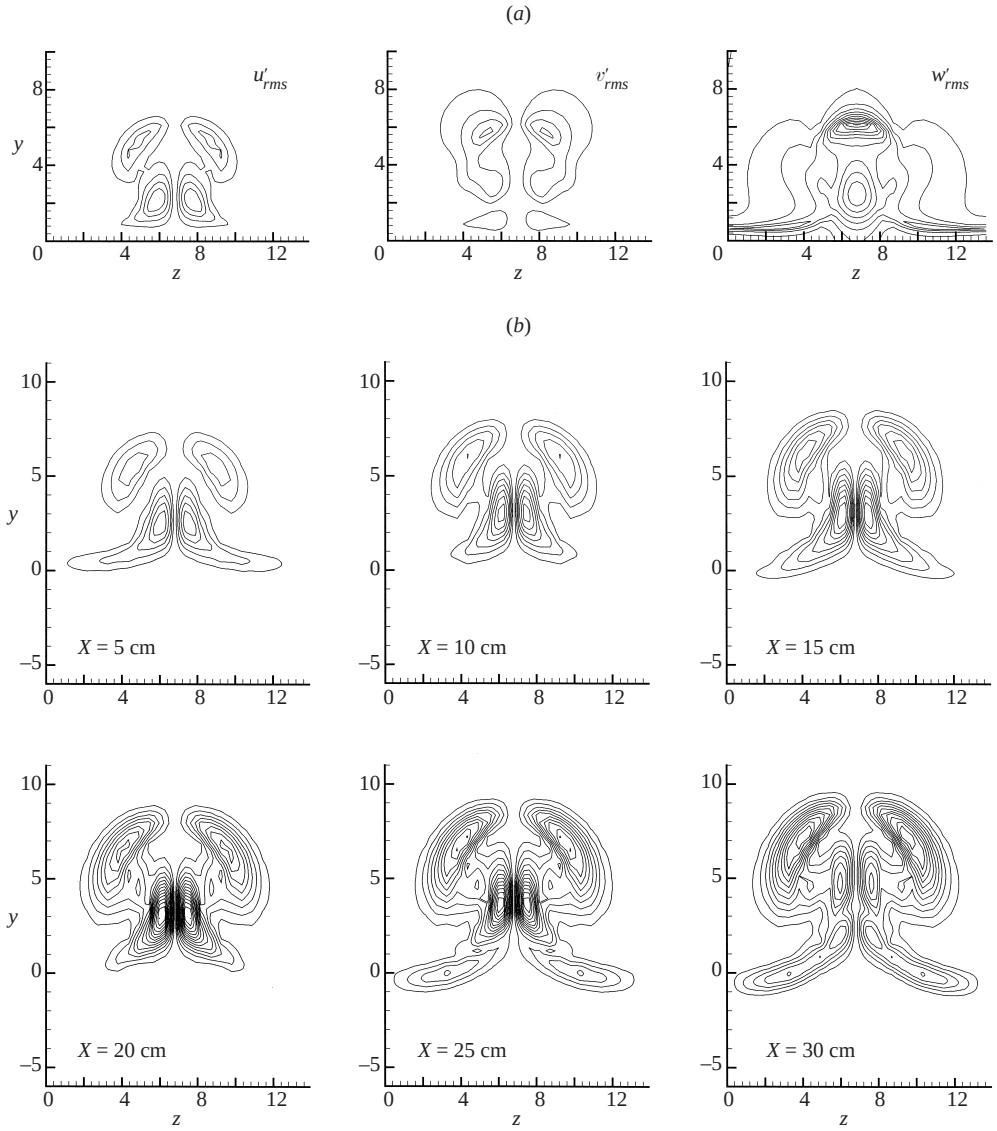

FIGURE 11. Nonlinear development of the r.m.s. of the secondary instability velocities in the cross-sectional (y, z)-plane in the mixing region as a function of the streamwise distance: outer contour value is 0.01 with increments of 0.01. (a) Initial mixing conditions $X_g = 90\,\text{cm}$, (b) u'_{rms}, (c) v'_{rms}, (d) w'_{rms}.

u'_{rms} is associated with the intense $\partial u/\partial z$ located on both sides of the shoulders and the stems of the iso-u mushroom contours. We see below that the structure of u'_{rms} is further explained via energy-conversion mechanisms.

The contours of the total steady streamwise velocity u in the mixing region are shown in figure 13 for a number of different downstream locations. These are the iso-u contours of the optimal steady flow longitudinal vorticity elements that are modified by the nonlinear secondary instability. The modified contours here should be compared to the unmodified steady flow problem without secondary instability shown in figure 3. In terms of energy transfer, the modified iso-u contours are slightly

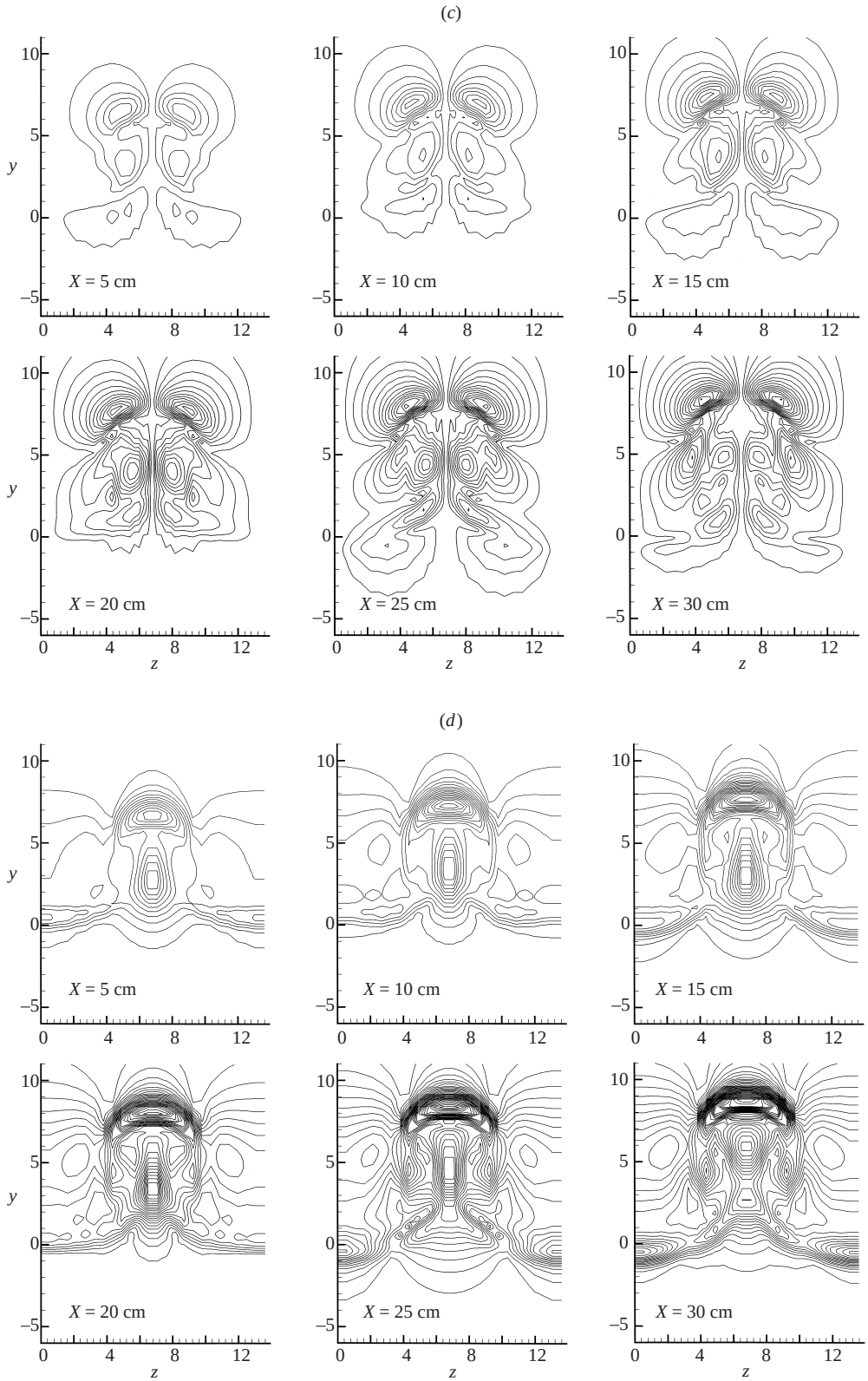

FIGURE 11(*c*, *d*). For caption see facing page.

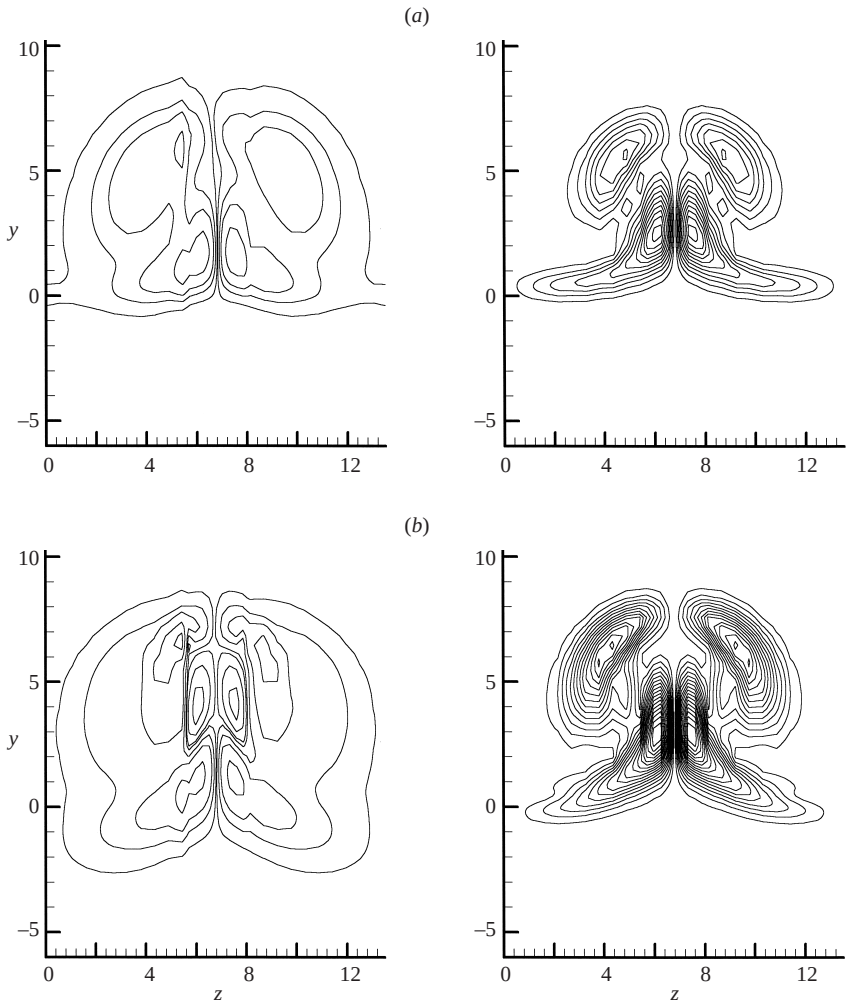

FIGURE 12. Contours of mean flow rate of strain, $\partial u/\partial z$ (left) and the fundamental sinuous mode secondary instability r.m.s. streamwise velocity u'_{rms} (right) in the mixing region. (*a*) $X = 5\,\text{cm}$, (*b*) $X = 15\,\text{cm}$.

asymmetrical about the z-axis in figure 13. However, they are symmetrical about the line of symmetry in z in the linear region of secondary instability. They are no longer 'perfectly' symmetrical in the nonlinear region due to the nonlinear interactions with the finite-amplitude secondary instability through the divergence of Reynolds stresses in the momentum equations (4.4)–(4.6). Since u' and v' are changing in z as $\sin(m\beta z)$ and w' is changing as $\cos(m\beta z)$, u'^2, v'^2, w'^2 and $u'v'$ are symmetrical, but both $u'w'$ and $v'w'$ are asymmetrical about $z = 0$. This asymmetrical behaviour and the asymmetrical z-derivatives manifest themselves explicitly as asymmetrical 'sources' in the momentum equations.

In the mixing region the nonlinear secondary instability significantly modifies the mushroom shape of the steady streamwise velocity iso-u contours as they develop downstream, as shown in figure 13. The upper region of the iso-u contours is severely modified by the strengthening u'_{rms} in the same region of figure 11. As shown by Yu & Liu (1994) in the linear theory, energy from $u^2/2$ goes directly to $u'^2/2$

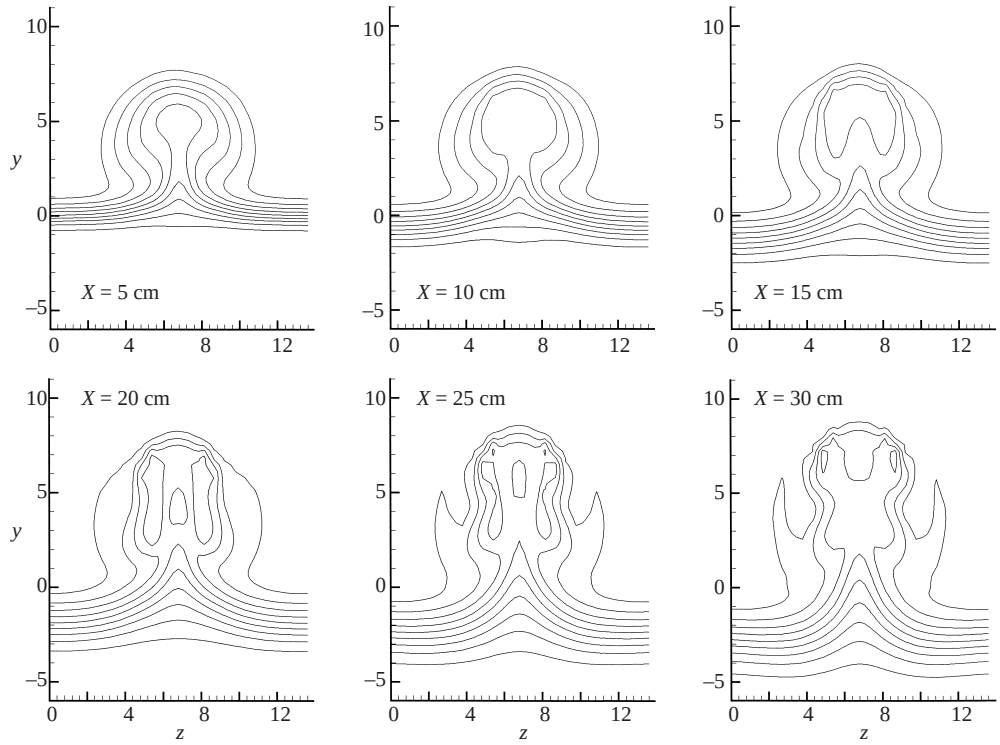

FIGURE 13. Nonlinear development of the total streamwise velocity contours in the cross-sectional (y, z)-plane in the mixing region. Outer contour has value 0.9 with a decrease of 0.1.

predominantly via the $-u'w'\partial u/\partial z$ energy-conversion mechanism for the sinuous mode. The contours of the dominant energy-conversion mechanism $u'w'\partial u/\partial z$, as well as of $u'v'\partial u/\partial y$, are shown in figures 14(a) and 14(b), respectively. Regions of intensive energy-conversion coincide with depletion of u and intensification of u'_{rms}. The regions near the base of the modified iso-u mushroom appear to be broadened in figure 13, as u'_{rms} (figure 11b) weakens in the same region, where energy is locally returned to $u^2/2$ from the secondary instability (figure 14). Note that the secondary instability structures in figure 11 do not protrude very far below the $y = 0$ line; however, the modified u protrudes farther into the bottom of the shear layer than the unmodified u (figure 13). This could be interpreted as enhanced momentum diffusivity for u due to the cumulative effects of momentum transfer by the 'microstructure' of the secondary instability.

5.2. *The role of secondary instability in mixing enhancement*

The spanwise-average profile of the mean flow, $\bar{u}$, is obtained but not shown. The resulting S-shaped inflectional profile is generated from the vortices upward advection of the low-momentum fluid, which still persists well into the mixing region. The secondary instabilities increase the mixing enhancement since $\bar{u}$, in the upper mixing region, reaches the value of 1.0 at shorter streamwise distances and spreads further into the lower mixing region.

The mixing enhancement parameters $\bar{u}_{cl}$, η and M are computed from the modified steady flow and are compared with the results from § 3 in order to assess the role of the secondary instability in the mixing enhancement process. Figure 4 compares

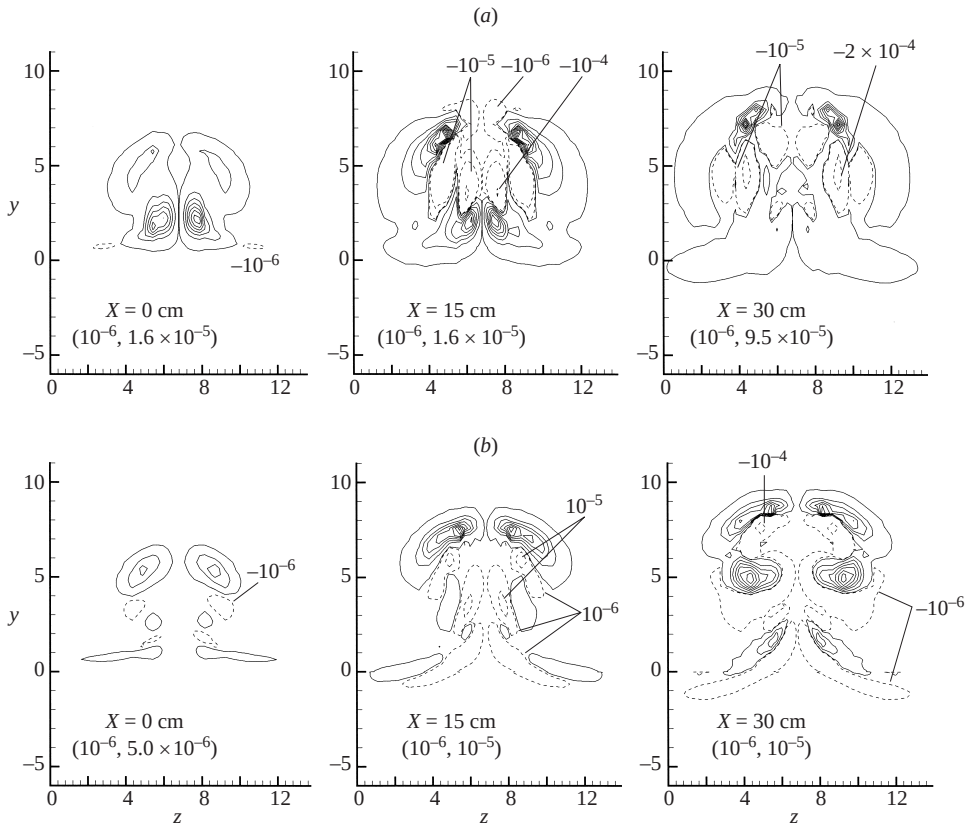

FIGURE 14. Contours of the dominant energy-conversion mechanism. Values are indicated as (outer contour value, increment). (*a*) $u'w'\partial u/\partial z$. (*b*) $u'v'\partial u/\partial y$.

the centreline value of the streamwise velocity, $\bar{u}_{cl}$ (dashed line), to the same velocity without the effect of the secondary instability (solid lines). Predictably, the centreline velocity increases dramatically and reaches the value of 0.83 at 30 cm behind the wall trailing edge, an increase of almost 50% over the results in § 3.

The mixing efficiency is shown in figure 5. The secondary instability increases the mixing efficiency by about 750% to $\eta \approx 5.0$. This is due in part to the increase in the value of the streamwise vorticity, ω_x. For example, 30 cm downstream in the mixing region, the circulation (calculated for one of the counter-rotating vortices) increase from to $0.104\,\mathrm{m^2\,s^{-1}}$ to $0.333\,\mathrm{m^2\,s^{-1}}$. Moreover, the mixedness parameter is increased by almost 100%, as shown in figure 6.

5.3. *Global energy-balance mechanisms: energies of the secondary instability and of the modified steady flow*

The kinetic energy equations for the disturbance velocity components (u', v', w') are obtained from the momentum equations for the nonlinear secondary instabilities. Rather than obtaining the energy balance from the scaled and simplified momentum equations (4.12)–(4.14), we use the full equations so that we can assess unimportant scaled mechanisms. Consequently, the total kinetic-energy-advection equation for $e = (u'^2 + v'^2 + w'^2)/2$ is obtained. Since the secondary instability develops spatially downstream, the Reynolds averages, as discussed in § 4, are defined as averages in

time. Accordingly, the time-averaged total kinetic-energy-advection equation can be written as follows:

$$\mathrm{d}E_u/\mathrm{d}x = I_p - I_d + I_{vd} + I_{td}, \tag{5.1}$$

where

$$E_u = \int_{-\infty}^{\infty}\int_0^{\lambda} u\bar{e}\,\mathrm{d}z\,\mathrm{d}y$$

is the secondary-instability energy-advection integral, $\bar{e}$ is the time average of e, and λ is the spanwise wavelength. The production, or more precisely, the energy-exchange integral is

$$I_p = -\int_{-\infty}^{\infty}\int_0^{\lambda}\left(\overline{u'^2}\frac{\partial u}{\partial x} + \overline{v'^2}\frac{\partial v}{\partial y} + \overline{w'^2}\frac{\partial w}{\partial z} + \overline{u'v'}\left(\frac{\partial u}{\partial y} + \frac{\partial v}{\partial x}\right) + \overline{u'w'}\left(\frac{\partial u}{\partial z} + \frac{\partial w}{\partial x}\right) + \overline{v'w'}\left(\frac{\partial v}{\partial z} + \frac{\partial w}{\partial y}\right)\right)\mathrm{d}z\,\mathrm{d}y, \tag{5.2}$$

the viscous dissipation integral is

$$I_d = \frac{1}{Re}\int_{-\infty}^{\infty}\int_0^{\lambda}\left(\begin{array}{l}\overline{\left(\dfrac{\partial u'}{\partial x}\right)^2} + \overline{\left(\dfrac{\partial u'}{\partial y}\right)^2} + \overline{\left(\dfrac{\partial u'}{\partial z}\right)^2} + \overline{\left(\dfrac{\partial v'}{\partial x}\right)^2} + \overline{\left(\dfrac{\partial v'}{\partial y}\right)^2} \\ \quad + \overline{\left(\dfrac{\partial v'}{\partial z}\right)^2} + \overline{\left(\dfrac{\partial w'}{\partial x}\right)^2} + \overline{\left(\dfrac{\partial w'}{\partial y}\right)^2} + \overline{\left(\dfrac{\partial w'}{\partial z}\right)^2}\end{array}\right)\mathrm{d}z\,\mathrm{d}y, \tag{5.3}$$

the streamwise viscous diffusion of secondary instability energy is

$$I_{vd} = \frac{1}{Re}\frac{\mathrm{d}^2}{\mathrm{d}x^2}\int_{-\infty}^{\infty}\int_0^{\lambda}\bar{e}\,\mathrm{d}z\,\mathrm{d}y, \tag{5.4}$$

and the 'turbulent' diffusion of secondary instability energy is

$$I_{td} = -\frac{\mathrm{d}}{\mathrm{d}x}\int_{-\infty}^{\infty}\int_0^{\lambda}\overline{u'(p'+e)}\,\mathrm{d}z\,\mathrm{d}y. \tag{5.5}$$

The left-hand side of (5.1) represents the streamwise rate of change of the streamwise advection of total kinetic energy, $\mathrm{d}E_u/\mathrm{d}x$. In spatially developing disturbances, it is the increase or decrease of E_u that is dictated by the energy balances rather than the total secondary instability kinetic energy E_{si} itself, where E_{si} is defined as

$$E_{si} = \int_0^{\lambda}\int_{-\infty}^{\infty}\bar{e}\,\mathrm{d}y\,\mathrm{d}z \tag{5.6}$$

for the mixing region. In temporally developing disturbances (Sabry & Liu 1991; Liu & Domaradzki 1993; Park & Huerre 1995), it is precisely E_{si} that is determined by the energy-balancing mechanisms that are similar, though not identical, to the right-hand side of (5.1). There, the streamwise-periodic averaging replaces the time average in which the streamwise diffusion mechanisms, (5.4) and (5.5), are absent.

The energy production or energy exchange mechanism in (5.2) was evaluated using the solution of the full momentum equations for the fundamental component. The total production integral is shown as a solid line in figure 15. In the region $X < 17\,\mathrm{cm}$, $I_p > 0$, representing a net energy transfer from the steady flow to the

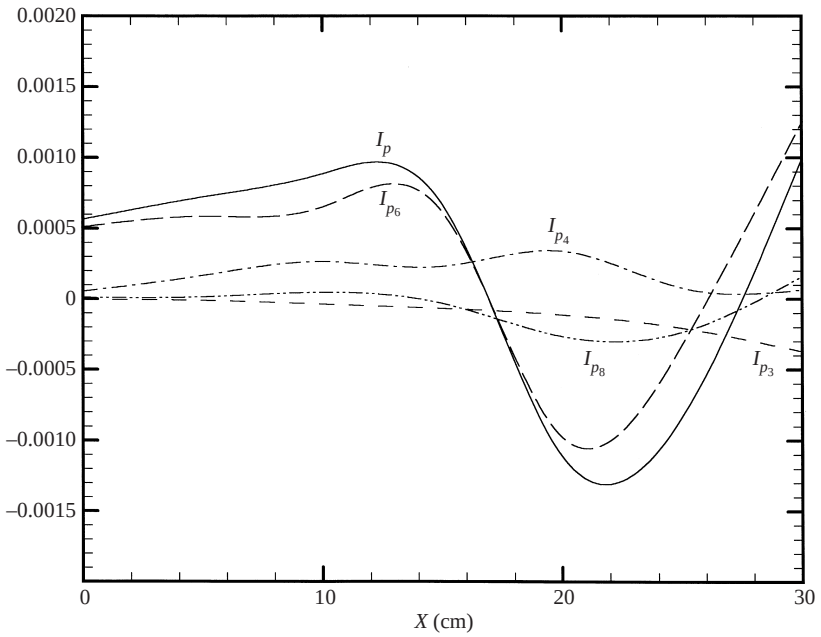

FIGURE 15. Energy production mechanisms.

secondary instability. In the region $X > 17\,\text{cm}$, $I_p < 0$, implying that net energy is transferred back to the steady flow from the secondary instability. In an 'inviscid' sense, the secondary instability becomes damped. Such a phenomenon is well known (see Liu 1988) in nonlinear instability of the Kelvin–Helmholtz type (with its dominant vorticity axis perpendicular to the streamwise direction) in spatially developing free-shear flows. The development of a positive then a negative production mechanism was first observed by Ko, Kubota & Lees (1970) in their theoretical and computational study of spatial development of finite disturbances in the laminar wake problem and was seen more recently in three-mode interactions in a mixing layer (Nikitopoulos & Liu 2001). Liu (1971) and Mankbadi & Liu (1981) noticed the same mechanism in the free turbulent shear flows.

The contributions to the total production integral in (5.2) were evaluated:

$$I_{p1} = -\int_{-\infty}^{\infty}\int_{0}^{\lambda}\left(\overline{u'^2}\frac{\partial u}{\partial x}\right)\mathrm{d}y\,\mathrm{d}z, \quad I_{p2} = -\int_{-\infty}^{\infty}\int_{0}^{\lambda}\left(\overline{v'^2}\frac{\partial v}{\partial y}\right)\mathrm{d}y\,\mathrm{d}z,$$

$$I_{p3} = -\int_{-\infty}^{\infty}\int_{0}^{\lambda}\left(\overline{w'^2}\frac{\partial w}{\partial z}\right)\mathrm{d}y\,\mathrm{d}z, \quad I_{p4} = -\int_{-\infty}^{\infty}\int_{0}^{\beta}\left(\overline{u'v'}\frac{\partial u}{\partial y}\right)\mathrm{d}y\,\mathrm{d}z,$$

$$I_{p5} = -\int_{-\infty}^{\infty}\int_{0}^{\beta}\left(\overline{u'v'}\frac{\partial v}{\partial x}\right)\mathrm{d}y\,\mathrm{d}z, \quad I_{p6} = -\int_{-\infty}^{\infty}\int_{0}^{\beta}\left(\overline{u'w'}\frac{\partial u}{\partial z}\right)\mathrm{d}y\,\mathrm{d}z,$$

$$I_{p7} = -\int_{-\infty}^{\infty}\int_{0}^{\lambda}\left(\overline{u'w'}\frac{\partial w}{\partial x}\right)\mathrm{d}y\,\mathrm{d}z, \quad I_{p8} = -\int_{-\infty}^{\infty}\int_{0}^{\lambda}\left(\overline{v'w'}\frac{\partial v}{\partial z}\right)\mathrm{d}y\,\mathrm{d}z,$$

$$I_{p9} = -\int_{-\infty}^{\infty}\int_{0}^{\lambda}\left(\overline{v'w'}\frac{\partial w}{\partial y}\right)\mathrm{d}y\,\mathrm{d}z.$$

Figure 15 shows the contributions to the total production integral I_p. The dominant contribution comes from I_{p6} for the sinuous fundamental mode, as expected. Except for small modifications, the total production integral I_p is very nearly tracked by I_{p6}. However, I_{p6} is supplemented by positive production due to the shear instability mechanism I_{p4}. These two production mechanisms were anticipated by the retention, through scale analysis, of the cross-sectional advection of the dominant steady-flow vorticity by the secondary instability in the x-momentum equation (4.12), $(v'\partial u/\partial y + w'\partial u/\partial z)$. These dominant mechanisms of mean vorticity advection, which lead to the dominant production mechanisms due to $\partial u/\partial z$ in I_{p6} and $\partial u/\partial y$ in I_{p4}, were identified earlier in wall-bounded secondary instability discussions (e.g. Sabry *et al.* 1990; Yu & Liu 1991, 1994).

Also shown in figure 15 are I_{p3} and I_{p8}, which are nearly zero during the net amplifying stage ($I_p > 0$). In the later stages of development where I_p has changed sign to $I_p < 0$, both I_{p3} and I_{p8} become active, though negligibly compared to I_{p6}, in augmenting the negative production mechanism of I_{p6}. There is a small X-region in which I_p reverts to positive production once again. Positive and negative production mechanisms are well known to prevail even in two-dimensional disturbances in two-dimensional developing free shear flows (e.g. see the discussions in Liu 1988).

The Reynolds number in the present context is $Re = 451.45$ and the overall viscous diffusion mechanism in (5.4), I_{vd}, is of the order 10^{-9} and is negligible compared with I_p values of about 10^{-3}–10^{-4}. In the absence of higher harmonics, the nonlinear stress term would not appear in the momentum equations of the fundamental component and thus the triple correlation terms reflecting 'turbulent diffusion' of e would be absent. In this case the surviving turbulent diffusion mechanism in (5.5) is

$$I_{td} = -\frac{\mathrm{d}}{\mathrm{d}x}\int_{-\infty}^{\infty}\int_{0}^{\beta}\overline{u'(p')}\,\mathrm{d}y\,\mathrm{d}z.$$

A numerical evaluation of the rate of change of the energy-advection integral, $\mathrm{d}E_u/\mathrm{d}x$, in (5.1) is shown in figure 16, along with I_p. Because of the large amount of data that could not be stored, the integrands of I_{td} and of the viscous dissipation integral, I_d, were not evaluated individually. However, their net effect can be obtained from (5.1) as $-(I_d - I_{td}) \cong \mathrm{d}E_u/\mathrm{d}x - I_p$. The behaviour of the net value of $-(I_d - I_{td})$ is also shown in figure 16. Since viscous dissipation is positive definite, $-I_d \leqslant 0$, the 'turbulent diffusion' effect I_{td} changes sign to play an important role downstream in balancing the net negative and then positive production in the downstream region. In this case $\mathrm{d}E_u/\mathrm{d}x$ reaches nearly constant values in the region computed.

E_{si}, the total secondary instability kinetic energy defined in (5.6), is shown in figure 17. It amplifies linearly at first on the logarithmic scale, but the growth rate decreases downstream in the region, almost corresponding to the reversal in sign of I_p in figure 15, and increases somewhat again as $-(I_d - I_{td})$ increases to positive values that counteract I_p. Eventually E_{si} saturates at a value of about 10^{-3}. This behaviour is somewhat typical of nonlinear instability development in shear flows (e.g. Stuart 1960; Liu 1988). A less reliable indicator of instability wave growth is the maximum value of u'_{rms} at any point in the cross-sectional (y, z)-plane for each streamwise location; the quantity $u'_{rms})_{max}$, also shown in figure 17 for comparison, grows linearly in the initial regions but intensifies downstream until it reaches a maximum value of $(u'_{rms})_{max} \approx 0.14$: it then starts to decrease. Unlike E_u, or E_{si} in the temporal problem, $(u'_{rms})_{max}$ does not readily yield relations obtainable from conservation equations. However, $(u'_{rms})_{max}$ itself is easily measured experimentally.

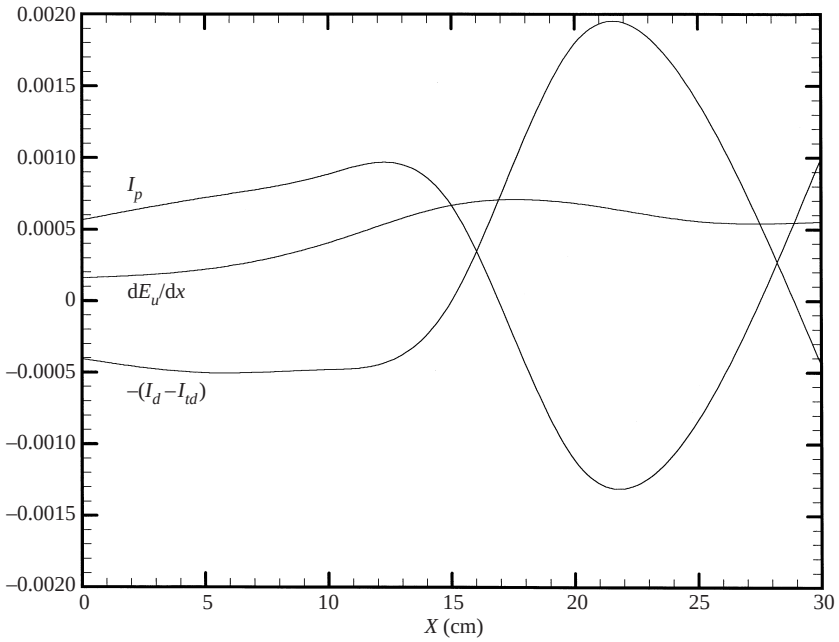

FIGURE 16. Advected secondary instability energy balance and development in the mixing region.

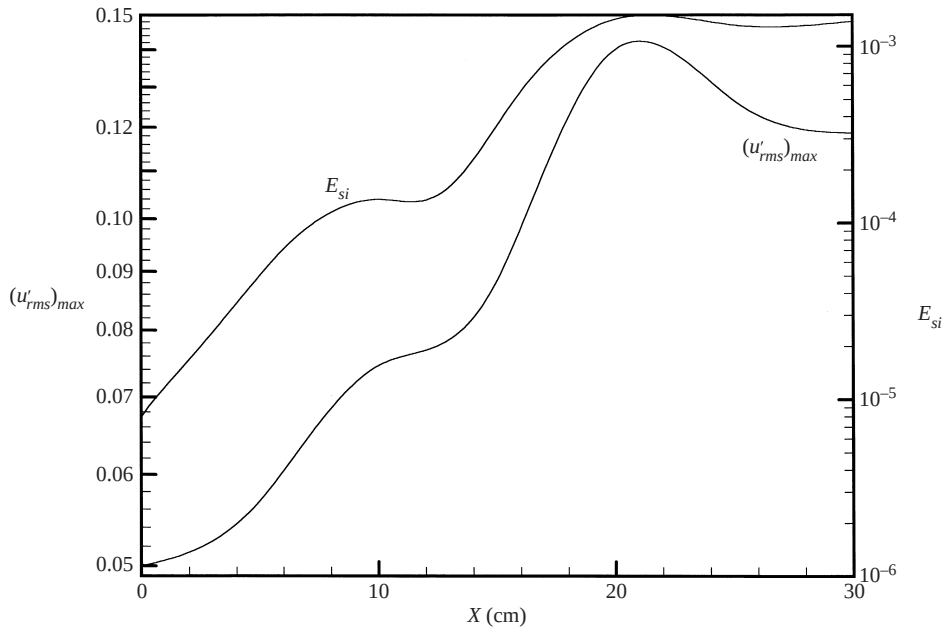

FIGURE 17. Nonlinear development of the maximum values of r.m.s. secondary instability streamwise velocity $(u'_{rms})_{max}$, and the total secondary instability energy E_{si} in the mixing region.

It was shown in § 5.1 that the steady flow 'mushrooms' were locally modified by the presence of the nonlinear secondary instability, particularly through the local energy-transfer mechanisms. The global energy of the steady flow without secondary instability, E, is shown in figure 9 for the optimal case (the line indicated by $X_g =$

90 cm). In comparison, the modified E due to secondary instability is also shown in figure 9 as a dashed line. As the production of secondary instability energy becomes intense in the early development, E therefore decreases. As the secondary instability returns energy back to the steady flow (see figure 15 and 16), E increases and then decreases again according to the changes in sign in the production mechanism (figure 16).

5.4. *The instantaneous mushroom oscillations*

Peerhossaini & Wesfried (1988) used light-sensitive fluorescent dye in a curved water channel to observe what appears to be the total flow structure of dye concentration in nonlinear Görtler vortices along the concave wall. The Schmidt number for fluorescene in water is of the order of 10^3, so that the concentration structure appears as very thin mushrooms but embedded in an iso-total streamwise velocity mushroom structure that is much broader (see, for instance, the discussion of scalar advection for this problem in Liu & Sabry 1991 and Liu & Lee 1995). In the order-unity Schmidt-number range for smoke seeding in air (Aihara, Tomita & Ito 1985; Ito 1985), the smoke patterns very nearly capture the full iso-streamwise velocity mushroom structure quantitatively measured by the hot wire (Swearingen & Blackwelder 1987). As already discussed, the analogy between dimensionless scalar advection and the streamwise velocity, for similar initial and boundary conditions, is complete for the steady problem for Prandtl and Schmidt numbers unity (Liu & Sabry 1991); but for the unsteady, secondary instability problem, the failure in the analogy lies in the streamwise pressure gradient due to the secondary instability fluctuations, unless one makes an artificially long-streamwise-wavelength approximation. However, even in the absence of exact analogies, it can still be conjectured that the oscillating scalar mushroom structure observed at a fixed streamwise location would somewhat resemble the total streamwise velocity structure for gases. In the case of large Schmidt number for liquids, the thin mushroom structure is embedded in a broader but invisible iso-streamwise velocity structure (Liu & Lee 1995). The oscillating mushrooms observed by Peerhossaini & Wesfried (1988) are indeed a manifestation of nonlinear secondary instability predominantly of the downstream-propagating wavy-sinuous mode (Hall & Horseman 1991; Yu & Liu 1991, 1994; Liu & Domaradzki 1993; Li & Malik 1995; Park & Huerre 1995). As such, light sheet observation (Peerhossaini & Wesfried 1988) at a given streamwise location over a perpendicular cross-section (in the (y, z)-plane) shows that the mushroom structure oscillates in the spanwise direction as the wave disturbance enters and leaves the fixed cross-sectional plane.

To depict such an oscillation of the total streamwise velocity that is nonlinearly modified by the secondary instability in the mixing region, the total iso-streamwise velocity contours of $u(y, z; x) + u'(y, z, t; x)$ are shown in figure 18 for one cycle of the oscillation. This depiction arises from the nonlinear calculations of the modified steady flow u and of the nonlinear secondary instability u'. To fix ideas, the cross sectional picture was taken at $X = 25$ cm measured from the trailing edge. From (4.2), the time scale is $T^* = \delta_0/U_0$ and the dimensionless time is $t = T/T^*$; the frequency is 130 Hz and the dimensionless frequency is $\sigma = 130\,\text{Hz}/2\pi T^* = 0.221$. The six plots correspond to $t = 0$, 5/24, 9/24, 13/24, 17/24, 21/24 of $2\pi/\sigma$. In real time, $T = tT^* = 0.00132/5\ t = 2.64 \times 10^{-4}\,t$ and varies from 0 to 7.5×10^{-3} s. The oscillations appear to be more vigorous in the high-speed region where the local mean rates of strain are the highest.

The computations were carried out with spanwise-periodic boundary conditions for a single mushroom, and consequently the resulting oscillations are about a fixed

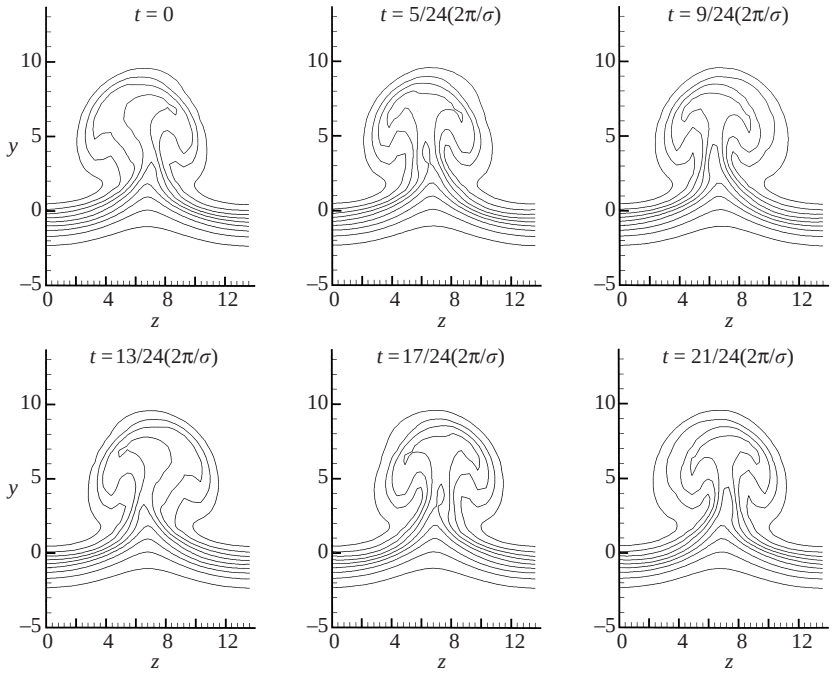

FIGURE 18. Nonlinear development of the total streamwise velocity (steady plus the unsteady secondary instability velocity) at different times, at the $X = 25\,\text{cm}$ cross-section in the mixing region. Outer contour has value 0.9 with a decline of 0.1.

mushroom base. In actual experiments in wall-bounded flow, Peerhossaini & Wesfried (1988) observed that the mushroom bases are also subject to oscillation. One can conjecture that in the mixing region the mushroom bases would also be subject to oscillations. In order to capture this feature of the base oscillations, the domain of numerical computations may well have to be expanded to include several of the mushroom structures in the initial streamwise region.

6. Concluding remarks

The formulation and numerical computation of the nonlinear development of steady Görtler vortices and their most amplified secondary instability in a mixing region have been developed and the results are used to understand their role in the mixing enhancement process. Quantitative assessment of mixing enhancement is made through the mixing efficiency and mixedness (and stretching of the interfacial surface in the steady case). Through the study of these parameters the optimal design can be determined, depending on the nature of the problem and the purpose of the mixing process. It is found that significant mixing enhancement can be achieved. In order to avoid the associated penalties of trailing-edge deformation, it will be beneficial to examine the use of the present concept in different geometrical situations, for example, round and rectangular jets, to bring the present class of studies closer to applications.

The present work studied a basically laminar reference flow over which entrainment and mixing enhancement through longitudinal vortices occur. The latter are essentially unstable 'transitional' structures whose streamwise lifetime is great enough to enhance mixing. The flows in real applications are most likely to be in the turbulent shear flow region. Even in turbulent shear flows, similar structures can be excited as they

are manifestations of shear flow instabilities that are augmented by turbulent rather than viscous dissipation (e.g. Liu 1988).

In wall-bounded flows, Tani (1962) found that longitudinal vortices, following a fixed spanwise wavelength, regenerate themselves even as the boundary layer became turbulent. Tani's argument is that the local Görtler number and wavenumber increases at a fixed wavelength continue until the boundary layer becomes turbulent. Then the appropriate 'eddy viscosity' of the turbulent flow lowers the local Görtler number and wavenumber, so that amplified longitudinal vortices develop again, but in a turbulent flow. Bradshaw (1973) discussed many interesting phenomena in turbulent flow as a result of streamline curvature. The observed large-scale coherent longitudinal vortices in concavely curved turbulent boundary layers in low-speed flow (So & Mellor 1975; Tani 1992) and in high-speed flow (Zakkay & Calarasee 1972) warrant further systematic studies of the repetition of Görtler instability in turbulent shear flows. Turbulent Taylor–Couette flow was observed much earlier by Pai (1939, 1943) and MacPhail (1941, 1946), in the earliest observations of 'coherent structures' in turbulent shear flows. Spanwise perturbations on turbulent mxing layers were experimentally studied by McCormick (1992) and Bell & Metha (1992, 1993). The details of the interaction between large-scale, coherent longitudinal vorticity elements and fine-grained turbulence may well be approached as in Liu (1988) for disturbances with axis normal to the main shear in which turbulence is given its own inertia. Thus it may be possible to extend the present class of problems to the turbulent shear-flow region.

The generation of longitudinal vortices in the mixing region at the outset is intimately related to ideas in 'bypass transition' (see for instance Matsubara & Alfredson 2001), in which the streak structures are similar to the secondary instability structures here and in Yu & Liu (1991, 1994). In such studies, the smaller-scale secondary instabilities are brought about by the three-dimensional structure of intense strain rates of the basic steady flow, independent of any effects of streamline curvature at a much larger scale.

This work was partially supported by NASA Lewis Research Center Grant NAG3-2067 and National Science Foundation Grant INT-96-02043; I. G. G. gratefully acknowledges the partial support of a Simon Ostrach Graduate Fellowship in the Division of Engineering at Brown University; J. T. C. L. acknowledges the stimulating hospitality of the Transition Group at Institut für Aero- und Gasdynamik, Universität Stuttgart during a Sabbatical leave 2000–2001, in particular M. Kloker, U. Rist, S. Wagner and the 'Interaktives Arbeiten in der Grenzschichttransition' and F. R. Hama. Various aspects of this work were presented at Couette–Taylor Workshops in Paris (1997) and in Breman (1999), at the APS Annual Meetings of the Division of Fluid Dynamics (1997, 1998, 2000, 2001), at the 7th Intl Symposium on Flow Modeling and Turbulence Measurement (1998) and at the ASME Fluids Engineering Summer Meeting (2000). The work described in this paper is largely based on Parts I and II of I. G. G.'s PhD Thesis, where color-interpretations of contour plots are given.

In memorium, Charles W. Van Atta 1934–2001.

REFERENCES

Aihara, Y. 1962 Transition in an incompressible boundary layer along a concave wall. *Bull. Aerospace Res. Inst. Univ. Tokyo* **3**, 195–240.

Aihara, Y. & Koyama, H. 1981 Secondary instability of Görtler vortices: formation of periodic three-dimensional coherent structure. *Trans. Japan Soc. Aero. Space Sci.* **24**, 78–94.

Aihara, Y. & Koyama, H. 1982 Nonlinear development and secondary instability of Görtler vortices. In *Stability in the Mechanics of Continua* (ed. F. H. Schroeder), pp. 210–220. Springer.

Aihara, Y., Tomita, Y. & Ito, A. 1985 Generation, development and secondary instability of Görtler vortices. In *Laminar-Turbulent Transition, IUTAM Symp. Novosibirsk-1984*. (ed. V. V. Kozlov), pp. 447–454. Springer.

Bassom, A. P. & Seddougui, S. 1990 The onset of three-dimensionality and time-dependence in Görtler vortices: neutrally stable wavy modes. *J. Fluid Mech.* **220**, 664–672.

Bell, J. H. & Mehta, R. D. 1992 Measurements of streamwise vortical structures in a plane mixing layer. *J. Fluid Mech.* **239**, 213–248.

Bell, J. H. & Mehta, R. D. 1993 Effects of imposed spanwise perturbations on plane mixing-layer structure. *J. Fluid Mech.* **257**, 33–63.

Benmalek, A. 1993 Nonlinear development of Görtler vortices over variable curvature walls. PhD Thesis, Arizona State Univ. Tempe.

Benmalek, A. & Saric, W. S. 1994 Effect of curvature variations on the nonlinear evolution of Görtler vortices. *Phys. Fluids* **6**, 3353–3367.

Bertolotti, F. P., Herbert, TH. & Spalart, P. R. 1992 Linear and nonlinear stability of the Blasius boundary layer. *J. Fluid Mech.* **242**, 441–474.

Bippes, H. 1972 Experimentelle Untersuchung des laminar-turblenten Umschlags as einer parallel angeströmten könkaven Wand. *Sitzungsherichte der Heidelberger Akademie der Wissenschaften Mathematischnaturwissenschaftliche Klasse* **3**, pp. 103–180 (also *NASA TM* -75243, 1978).

Bippes, H. & Görtler, H. 1972 Dreidimensionale störungen in der Grenzschicht an einer konkaven Wand. *Acta Mech.* **14**, 251–267.

Bradbury, L. J. S. & Khadem, A. H. 1975 The distortion of a jet by tabs. *J. Fluid Mech.* **70**, 801–813.

Bradshaw, P. 1973 Streamline curvature on turbulent flow. *AGARD* AG-169.

Carletti, M. J. & Rogers, C. B. 1995 Use of streamwise vorticity to increase mass entrainment in a cylindrical ejector. *AIAA J.* **9**, 1641–1645.

Chorin, A. 1967 A numerical method for solving incompressible viscous flow problems. *J. Comput. Phys.* **2**, 12–26.

Crouch, R. W., Coughlin, C. L. & Paynter, G. C. 1977 Nozzle exit flow profile shaping for jet noise control. *J. Aircraft* **14**, 860–867.

Debonis, J. R. 1992 Full Navier–Stokes analysis of a two-dimensional mixer/ejector nozzle for noise suppression. *NASA Tech. Memo.* 105715 (also *AIAA Paper* 92-3570).

Denier, J. P., Hall, P. & Seddougui, S. O. 1991 On the receptivity problem for Görtler vortices: Vortex motion induced by roughness. *Phil. Trans. R. Soc. Lond.* A **335**, 51–85.

Eckerle, W. A., Sheibani, H. & Awad, J. 1992 Experimental measurements of vortex development downstream of a lobed forced mixer. *Trans. ASME: J. Engrg. Gas Turbine and Power* **114**, 63–71.

Fiebig, M. 1996 Vortices and heat transfer. Z. *Angew. Math. Mech.* **76**, 1–16.

Floryan, J. M. 1991 On the Görtler instability of boundary layers. *Prog. Aerospace Sci.* **28**, 235–271.

Floryan, J. M. & Saric, W. S. 1982 Stability of Görtler vortices in boundary layers. *AIAA J.* **20**, 316–324.

Gaster, M. 1962 A note on the relation between temporally-increasing and spatially-increasing disturbances in hydrodynamic stability. *J. Fluid Mech.* **14**, 222–224.

Girgis, I. G. 2000 The use of Görtler vortices in mixing enhancement and their presence in the supersonic turbulent boundary layer. PhD Thesis, Brown University, Division of Engineering Providence.

Goldstein, M. E. & Mathew, J. 1993 The development of a mixing layer under the action of weak streamwise vortices. *Phys. Fluids* A **5**, 600–607.

Görtler, H. 1940 Über eine dreidimensionale instabilität laminarer Grenzschichten an Konkaven Wänden. *Nachr. Ges. Wiss. Göttingen, Math. Phys. Klasse, Neue Folge* **2**, 1–26 (also NACA TM 1375, 1954).

Grosch. C. E., Seiner, J. M. Hussaini, M. Y. & Jackson, T. L. 1997 Numerical simulation of mixing enhancement in a hot supersonic jet. *Phys. Fluids* **9**, 1125–1143.

Hall, P. 1983 The linear development of Görtler vortices in growing boundary layers. *J. Fluid Mech.* **130**, 41–58.

Hall, P. 1988 The nonlinear development of Görtler vortices in growing boundary layers. *J. Fluid Mech.* **193**, 243–266.

Hall, P. & Horseman, N. J. 1991 The inviscid secondary instability of longitudinal vortex structures in boundary layers. *J. Fluid Mech.* **232**, 357–375.

Hall, P. & Seddougui, S. 1989 On the onset of three-dimensionality and time dependence in the Görtler vortex problem. *J. Fluid Mech.* **204**, 405–420.

Hämmerlin, G. 1955 Uber das Eigenwertproblem der dreidimensipnalen Instabilitat Laminarer Grenzschichten an konkaven Wanden. *J. Rat. Mech. Anal.* **4**, 279–321.

Herbert, T. 1997 Parabolized stability equations. *Annu. Rev. Fluid Mech.* **29**, 245–283.

Ho, C. M. & Huerre, P. 1984 Perturbed free shear layers. *Annu. Rev. Fluid Mech.* **16**, 365–424.

Ito, A. 1980 The generation and breakdown of longitudinal vortices along a concave wall. *J. Japan Soc. Aero. Space Sci.* **28**, 327–333.

Ito, A. 1985 Breakdown structure of longitudinal vortices along a concave wall. *J. Japan Soc. Aero. Space Sci.* **33**, 166–172.

Ito, A. 1988 On the relation of horshoe-type vortices and fluctuating flows. *J. Japan Soc. Aero. Space Sci.* **36**, 274–279.

Karasso, P. S. & Mungal, M. G. 1997 Mixing and reaction in curved liquid shear layers. *J. Fluid Mech.* **334**, 381–409.

Kaufman, L. C. 1975 The LZ algorithm to solve the generalized eigenvalue problem for complex matrices. *ACM Trans. Math. Software* **1**, 271–281.

Ko, D. R. S., Kubota, T. & Lees, L. 1970 Finite disturbance effect in the stability of laminar incompressible wake behind a flat plate. *J. Fluid Mech.* **40**, 315–341.

Lasheras, J. & Choi, H. 1988 Three dimensional instability of a plane free shear layer: an experimental study of the formation and evolution of streamwise vortices. *J. Fluid Mech.* **189**, 53–86.

Lee, K. & Liu, J. T. C. 1992 On the growth of mushroom like structures in nonlinear spatially developing Görtler vortex flow. *Phys. Fluids* A **4**, 95–103.

Li, F. & Malik, R. M. 1995 Fundamental and subharmonic secondary instabilities of Görtler vortices. *J. Fluid Mech.* **297**, 77–100.

Lin, C. C. 1955 *The Theory of Hydrodynamic Stability*. Cambridge University Press.

Liou, W. W. 1994 Linear instability of curved free shear layers. *Phys. Fluids* **6**, 541–549.

Liu, J. T. C. 1971 Nonlinear development of an instability wave in a turbulent wake. *Phys. Fluids* **14**, 2251–2257.

Liu, J. T. C. 1988 Contributions to the understanding of large-scale coherent structures in developing free turbulent shear flows. *Adv. Appl. Mech.* **26**, 183–309.

Liu, J. T. C. 1998 The role of controlled longitudinal vortices on transport. In *Proc 7th Intl Symp. Flow Modeling and Turbulence Measurements*, National Cheng Kung Univ. Tainan, October 5–6, 1998, pp. 589–607.

Liu, J. T. C. & Lee, K. 1995 Heat transfer in a strongly nonlinear spatially developing longitudinal vorticity system. *Phys. Fluids* **7**, 559–599.

Liu, J. T. C. & Sabry, A. S. 1991 Concentration and heat transfer in nonlinear Görtler vortex flow and the analogy with longitudinal momentum transfer. *Proc. R. Soc. Lond.* A **432**, 1–12.

Liu, W. 1991 Direct numerical simulation of transition to turbulence in Görtler flow. PhD Thesis, Univ. Southern California, Los Angeles.

Liu, W. & Domaradzki, A. 1990 *AIAA Paper* 90-0114.

Liu, W. & Domaradzki, A. 1993 Direct numerical simulation of transition to turbulence in Görtler flow. *J. Fluid Mech.* **240**, 267–309.

MacPhail, D. C. 1941 Turbulence in a distorted passage and between rotating cylinders. PhD Thesis, Univ. Cambridge (also in *Proc. 6th Intl Congr. Appl. Mech. Paris, 1946*).

Mankbadi, R. & Liu, J. T. C. 1981 A study of the interactions between large-scale coherent structures and fine-grained turbulence in a round jet. *Phil. Trans. R. Soc. Lond.* A **298**, 541–602.

Margolis, D. P. & Lumley, J. L. 1965 Curved turbulent mixing layer. *Phys. Fluids* **8**, 1775–1784.

Matsubara, M. & Alfredson, P. H. 2001 Disturbance growth in boundary layers subjected to free-stream turbulence. *J. Fluid Mech.* **430**, 149–168.

McCormick, D. C. 1992 Vortical and turbulent structure of planar and lobed mixer free-shear layers. PhD Thesis, University of Connecticut.

McCormick, D. C. & Bennett, JR., J. C. 1994 Vortical and turbulent structure of a lobed mixer free shear layer. *AIAA J.* **32**, 1852–1859.

McVey, J. B. 1998 Observation of the effect of streamwise vorticity on the spreading of flames in high speed flow. *Combust. Sci. Tech.* **60**, 447–451.

Mitchell, M. G., Smith, L. L., Karagozian, A. R. & Smith, O. I. 1996 NO_x emissions from a lobed fuel injector/burner. *Western States Section/The Combustion Institute Fall Meeting, October 1966.* Paper 96F-075.

Naughton, J. W. & Settles, G. S. 1992 Experiments on the enhancement of compressible mixing via streamwise vorticity. Part I. Optical measurements. *AIAA Paper* 92-3549.

Nikitopoulos, D. E. & Liu, J. T. C. 2001 Nonlinear three-mode interactions in a developing mixing layer. *Phys. Fluids* **13**, 966–982.

Novopashin, S. A. & Perepelkin, A. L. 1989 Axial symmetry loss of a supersonic pre-turbulent jet. *Phys. Lett.* A **135**, 290–293.

Otto, S. R., Jackson, T. L. & Hu, F. Q. 1996 On the spatial evolution of centrifugal instabilities within curved incompressible mixing layers. *J. Fluid Mech.* **315**, 85–103.

Pai, S. I. 1939 Turbulent flow between rotating cylinders. PhD Thesis, California Inst. Technology, Pasadena (also *NACA Tech. Note* 892, 1943).

Park, D. S. 1990 The primary and secondary instabilities of Görtler flow. PhD Thesis, Univ. Southern California, Los Angeles.

Park, D. S. & Huerre, P. 1995 Primary and secondary instabilities of the asymptotic suction boundary layer on a curved plate. *J. Fluid Mech.* **283**, 249–272.

Peerhossaini, H. & Wesfreid, J. E. 1988 On the inner structure of streamwise Görtler rools. *Intl J. Heat Fluid Flow* **9**, 12–18.

Presz, W. M., Gousy, R. & Morin, B. L. 1986 Forced mixer lobes in ejector designs. *AIAA Paper* 86-1614.

Rao, G. V. R. & Heiba, A. A. 1990 Use of secondary flows for rapid mixing in scramjet combustors. *AGARD Hypersonic Combined Cycle Propulsion – Spain.*

Sabry A. S. 1988 Numerical computation of the nonlinear evolution of Görtler vortices. PhD Thesis, Brown University, Providence.

Sabry, A. S. & Liu, J. T. C. 1988 Nonlinear development of Görtler vortices and the generation of high shear layers in the boundary layer. *Appl. Maths. Fluid Mech. and Astrophys, Symp in Honor of C. C. Lin – 1987* (ed. D. J. Benney, F. H. Shu & C. Yuen), pp. 175–183. World Scientific.

Sabry, A. S. & Liu, J. T. C. 1991 Longitudinal vorticity elements in boundary layers: nonlinear development from initial Görtler vortices as a prototype problem. *J. Fluid Mech.* **231**, 615–663.

Sabry, A. S., Yu, X. & Liu, J. T. C. 1990 Secondary instabilities of three-dimensional inflectional velocity profiles resulting from longitudinal vorticity elements in boundary layers. In *Laminar–Turbulent Transition – 1989* (ed. D. Arnal & E. Michel), pp. 441–451. Springer.

Saric, W. S. 1994 Görtler vortices. *Annu. Rev. Fluid Mech.* **26**, 379–409.

Schadow, K. C., Gutmark, E., Koshigoe, S. & Wilson, K. J. 1989 Combustion-related shear flow dynamics in elliptic supersonic combustion. *AIAA J.* **27**, 1347–1353.

Smith, L. L., Majamski, A. J., Lam, I. T., Delabroy, O., Karagozian, A. R., Marble, F. E. & Smith, O. I. 1997 Mixing enhancement in a lobed injector, *Phys. Fluids* **9**, 667–678.

So, R. M. C. & Mellor, G. L. 1975 Turbulent boundary layers on curved walls. *Aero. Q.* **26**, 25–40.

Strickland, J. H., Selerland, T. & Karagozian, A. R. 1998 Numerical simulation of a lobed fuel injector, Part I: Non-reactive flow. *Phys. Fluids* **10**, 1950–2964.

Stuart, J. T. 1956 On the effects of the Reynolds stress on hydrodynamic stability. *Z. Angew. Math. Mech.* Sonderheft, S32–S38.

Stuart, J. T. 1958 On the nonlinear mechanics of hydrodynamic stability. *J. Fluid Mech.* **4**, 1–21.

Stuart, J. T. 1960 On the nonlinear mechanics of wave disturbances in stable and unstable parallel flows. Part 1. The basic behaviour in plane Poiseuille flow. *J. Fluid Mech.* **9**, 353–370.

Stuart, J. T. 1962*a* Nonlinear effects in hydrodynamic stability. In *Proc. Xth Intl Congr. Appl. Mech., Stresa, 1960*, pp. 63–97. Elsevier.

Stuart, J. T. 1962*b* On the three-dimensional nonlinear effects in the stability of parallel flow. *Adv. Aero. Sci.* **3**, 121–142.

Swearingen, J. D. & Blackwelder, R. F. 1987 The growth and breakdown of streamwise vortices in the presence of a wall. *J. Fluid Mech.* **182**, 255–290.

Swithenbank, J., Eames, I., Chin, S., Ewan, B. & Yang, Z. 1989 Turblent mixing in supersonic combustion systems. *AIAA Paper* 89-0260.

Tani, I. 1962 Production of longitudinal vortices in the boundary layer along a concave wall. *J. Geophys. Res.* **67**, 3075–3080.

Tillman, T. G., Patrick, W. P. & Paterson, R. W. 1991 Enhanced mixing of supersonic jets. *J. Propul. Power* **7**, 1006–1014.

Tsui, Y. Y. & Wu, P. W. 1966 Investigation of the mixing flow structure in multilobe mixers. *AIAA J.* **34**, 1386–1391.

Waitz, I. A. & Underwood, D. S. 1996 Effect of heat release on streamwise vorticity enhanced mixing. *J. Propul. Power* **12**, 638–645.

Waitz, I. A., Qui, Y. J., Manning, T. A., *et al.* 1997 Enhanced mixing with streamwise vorticity. *Prog. Aerospace Sci.* **33**, 323–351.

Wang, C. 1984 The effects of curvature on turbulent mixing layers. PhD Thesis, California Institute of Technology, Pasadena.

Yarin, A. L., Kowalewski, T. A., Hiller, W. J. & Koch, S. 1996 Distribution of particles suspended in convective flow in differentially heated cavity. *Phys. Fluids* **8**, 1130–1140.

Yu, K. H., Kraeutle, K. H., Wilson, K. J. & Parr, T. P. 1992 Supersonic flow mixing and combustion using ramp nozzle. *AIAA Paper* 92-3840.

Yu, X. & Liu, J. T. C. 1991 The secondary instability of Görtler flow. *Phys. Fluids* A **3**, 1845–1847.

Yu, X. & Liu, J. T. C. 1994 On the mechanism of sinuous and varicose modes in three-dimensional viscous instability of Görtler rolls. *Phys. Fluids* **6**, 736–750.

Yu, S. C. M., Yeo, J. H. & Teh, K. L. 1995 Velocity measurements of a lobed-forced mixer with different trailing-edge configurations. *J. Propul. Power* **11**, 87–97.

Zakkay, V. & Calarsee, W. 1972 An experimental investigation of vortex generation in a turbulent boundary layer undergoing adverse pressure gradient. *NASA CR* 2037.

Zaman, K. B. M. Q., Reeder, M. F. & Samimy, M. 1994 Control of an axisymmetric jet using tabs, *Phys. Fluids* **6**, 778–793.